

Experimental impact features in Stardust aerogel: How track morphology reflects particle structure, composition, and density

Anton T. KEARSLEY^{1*}, Mark J. BURCHELL², Mark C. PRICE², Michael J. COLE²,
Penelope J. WOZNAKIEWICZ³, Hope A. ISHII³, John P. BRADLEY³, Marc FRIES⁴,
and Nicholas J. FOSTER⁵

¹Impacts and Astromaterials Research Centre, Department of Mineralogy, The Natural History Museum, London SW7 5BD, UK

²School of Physical Science, University of Kent, Canterbury CT2 7NH, UK

³Institute of Geophysics and Planetary Physics, Lawrence Livermore National Laboratory, Livermore, California 94550, USA

⁴Planetary Science Institute, 1700 East Fort Lowell, Suite 106, Tucson, Arizona 85719, USA

⁵SENCR-MIC, Fayetteville State University, Fayetteville, North Carolina 28301, USA

*Corresponding author. E-mail: a.kearsley@nhm.ac.uk

(Received 01 July 2011; revision accepted 28 March 2012)

Abstract—The Stardust collector shows diverse aerogel track shapes created by impacts of cometary dust. Tracks have been classified into three broad types (A, B, and C), based on relative dimensions of the elongate “stylus” (in Type A “carrots”) and broad “bulb” regions (Types B and C), with occurrence of smaller “styli” in Type B. From our experiments, using a diverse suite of projectile particles shot under Stardust cometary encounter conditions onto similar aerogel targets, we describe differences in impactor behavior and aerogel response resulting in the observed range of Stardust track shapes. We compare tracks made by mineral grains, natural and artificial aggregates of differing subgrain sizes, and diverse organic materials. Impacts of glasses and robust mineral grains generate elongate, narrow Type A tracks (as expected), but with differing levels of abrasion and lateral branch creation. Aggregate particles, both natural and artificial, of a wide range of compositions and volatile contents produce diverse Type B or C shapes. Creation of bulbous tracks is dependent upon impactor internal structure, grain size distribution, and strength, rather than overall grain density or content of volatile components. Nevertheless, pure organic particles do create Type C, or squat Type A* tracks, with length to width ratios dependent upon both specific organic composition and impactor grain size. From comparison with the published shape data for Stardust aerogel tracks, we conclude that the abundant larger Type B tracks on the Stardust collector represent impacts by particles similar to our carbonaceous chondrite meteorite powders.

INTRODUCTION

Silica aerogel has proven to be an effective cosmic dust capture medium for deployment in space missions (Tsou et al. 1988, 1990; Tsou 1990, 1995; Zolensky et al. 1990; Barrett et al. 1992; Hörz et al. 1998, 2000; Burchell et al. 1999, 2001, 2006a, 2007, 2008a, 2008b, 2009). However, although some analytical techniques can be carried out in situ, in general, the postflight handling of aerogel, and the extraction of entire tracks or isolation of individual captured grains require great care (Westphal

et al. 2002, 2004; Ishii et al. 2005; Ishii and Bradley 2006). For a thorough review of the manufacture, physical properties, and applications of aerogel in hypervelocity particle capture, see Burchell et al. (2006). Earlier laboratory light-gas gun (LGG) experiments (Burchell and Thomson 1996; Hörz et al. 1998; Kitazawa et al. 1999) demonstrated that impacting grains leave distinctive penetration tracks, whose size depends on impactor mass and velocity, as well as the properties of the aerogel target. Impacts on the Orbital Debris Collector experiment deployed on the Mir space station (Hörz et al. 2000)

showed a range of track shape, originally attributed to major variation in impact velocity (rather than differences in the nature of the impactor) resulting in different levels of volatile release and consequent aerogel displacement. Subsequent laboratory experiments (e.g., Hörz et al. 2006) revealed that projectile properties, such as low density and structural weakness, could also control track morphology.

Aerogel was deployed as the primary capture medium on the NASA Stardust spacecraft, successfully collecting a large number of dust particles from comet 81P/Wild 2 (Brownlee et al. 2006; Hörz et al. 2006; Burchell et al. 2008a); all impacted at normal incidence with a very similar velocity, 6.1 km s^{-1} , yet producing a wide range of track shapes. Based on optical imagery, Hörz et al. (2006) classified Stardust track shape into three types, whose typical limiting dimensions were subsequently quantified by Burchell et al. (2008a): Type A, with an elongate and narrow stylus, which may divide and which usually have maximum width (MW) to total length (TL) ratios of <0.11 ; Type B, with an initial bulbous portion (we shall term this “proximal,” meaning near to the aerogel surface) with one or more styli far from the surface (in what we shall term the “distal” region) and which have MW:TL ratios between 0.11 and 0.35; Type C, broad and bulbous with no elongate styli and MW:TL ratios >0.35 . Figure 1 shows the typical form of the three track types found in Stardust aerogel, using examples from our experimental work to illustrate common and distinctive morphological features, and to define the measurements used in quantifying track dimensions. As well as confirming the basic tripartite classification, the very detailed shapes of Stardust tracks are now becoming apparent, especially with the use of high-resolution, three-dimensional imaging techniques such as laser scanning confocal microscopy (LSCM), (Kearsley et al. 2007; Greenberg and Ebel 2010) and synchrotron X-ray microtomography (Ebel et al. 2009; Tsuchiyama et al. 2009; Iida et al. 2010). Such studies have begun to reveal the true size and distribution of many fine-scale features such as minor styli, extensive off-track fracture systems appearing as curved, spiraling “petals,” and short lateral “spikes” (Fig. 1), all of which may contain impactor debris (e.g., Tsuchiyama et al. 2009). How such subtle structures develop, and their relationship with specific impactor properties, is clearly worthy of investigation.

Recent Experimental and Theoretical Investigation of Impact on Aerogel

Calibration to permit determination of impactor size from track dimensions was performed successfully by Burchell et al. (2008a), who used LGG shots of soda-lime glass projectiles of closely constrained size and

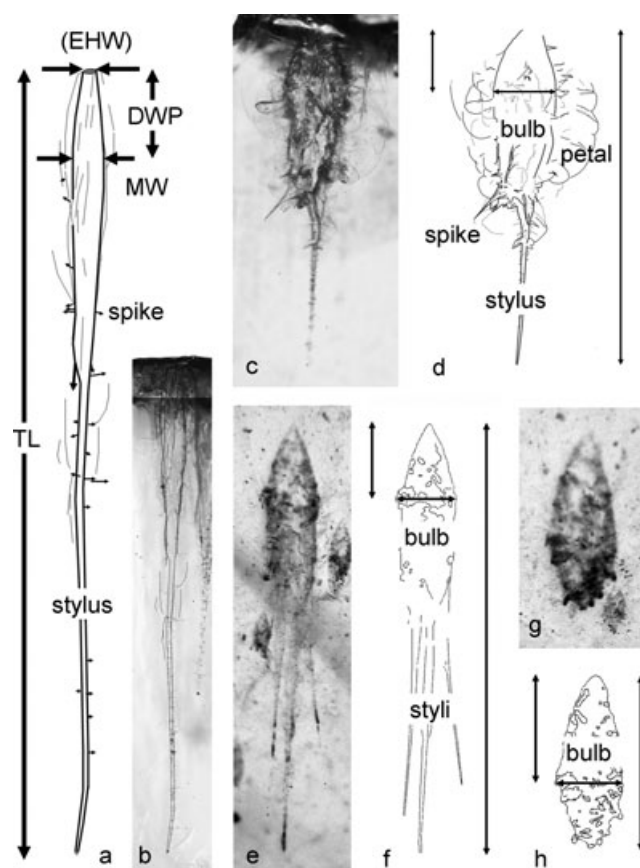


Fig. 1. Morphological terms applied to experimental aerogel impact tracks (analogous to Stardust cometary dust tracks in aerogel), optical images and line drawings: a, b) Type A; c–f) Type B; g, h) Type C. Measurements used in this paper for quantification of track shape (total length, TL, and maximum width, MW) follow conventions of Burchell et al. (2008a), although entrance hole width (EHW) and depth to widest point (DWP) are not employed in this present study. TL, MW, and DWP are also indicated in d, f, and h.

composition. These experiments provided a basis for understanding the length and width of simple tracks (Type A) in aerogel of specific density as a function of projectile diameter at a fixed impact velocity, and gave a good fit to a linear relationship. Niimi et al. (2011) have recently studied experimental impacts by a suite of particles of known sizes and differing densities, and in contrast to Burchell et al. (2008a), concluded that larger impactors can create disproportionately greater length and width of tracks in aerogel of constant density. Although Niimi et al. did not illustrate the morphology of their tracks, they also suggested that there is a relationship between impactor density and the relative shape of the resulting track, with higher density projectiles creating longer tracks, but with less increase in track width. They therefore proposed that track length/diameter might be used as an indication of

impactor density, extending this argument to more complex Type B and C track shapes. Whether widely differing particle internal strength and thermal stability across their range of projectile types (see Burchell et al. 2009b) might be more important than density as the primary control, was not discussed.

Domínguez et al. (2004) and Trigo-Rodríguez et al. (2008) have used theoretical physical models to explain how aerogel tracks may form. Experimental impact results from many LGG shots of robust projectiles, illustrated in many papers (e.g., minerals, Burchell et al. 2006; soda-lime glass, Hörz et al. 2006; Burchell et al. 1999, 2001, 2008a; alumina, Hörz et al. 2009; Niimi et al. 2011) have largely agreed with such models of simple Type A track formation. A curious type of short tapering tracks, similar in general outline to a squat Type A has now also been recognized (Nixon et al. 2012), being created by impact of the amino-acid glycine. Type B and C tracks have only been reproduced experimentally in a few unusual cases, e.g., by porous grains of the microcrystalline hydrous serpentine mineral lizardite, making small Type C and B tracks (Burchell et al. 2008a; Foster et al. 2008). Mixtures of robust glass grains with cocoa powder can also make Type B tracks, or cocoa powder alone may produce Type C (Hörz et al. 1998, 2006). Comparison of the models by Trigo-Rodríguez et al. (2008) with experimental data has begun to reveal how complex particle behavior is reflected in track shape, suggesting that mechanical deformation and break-up of aggregate impactors are the main mechanism responsible for Type C (and probably Type B) tracks, with expansion of volatile components playing little part. However, beyond this pioneering work, relatively few experimental results have been published concerning shape and size of more complex tracks. This is partly due to difficulties in creating and shooting appropriate composition projectile materials of known, uniform properties. For this reason, no illustrated catalog of the diverse experimental aerogel track shapes made by particles truly analogous to cometary dust components has yet been published.

The role of impactor properties in the creation of distinctive crater shapes on metal has now been extensively investigated in laboratory experiments using projectiles of well known composition (Kearsley et al. 2006, 2007; Hörz 2012). We have recently also successfully impacted artificial mineral aggregates (Kearsley et al. 2008, 2009) and diverse organic materials (Price et al. 2010) onto aluminum foils like those on Stardust, enabling us to link the observed crater shapes to broader knowledge of particle structure and composition. We tentatively suggested that Stardust aerogel track morphologies (A, B, and C) might be included in a combined scheme (fig. 11 in Kearsley et al.

2009), and to test this, we have now fired the same range of aggregate and organic projectiles onto aerogel.

In over a decade of experiments, we have accumulated many examples of hypervelocity impacts by a wide range of appropriate materials on aerogel, largely as a by-product of other work: assessing in situ analysis techniques (Burchell et al. 2001, 2004, 2006b; Graham et al. 2004, 2005; Kearsley et al. 2007); preservation of known composition particles after capture (Foster et al. 2007; Ishii et al. 2008; Marcus et al. 2008; Burchell et al. 2009b; Fries et al. 2009); and methods for extraction and preparation of captured grains (Graham et al. 2003; Ishii et al. 2005). In this article, we bring together illustrations of a wide range of aerogel track shapes, from shots of diverse particle types: single monomineralic grains and monomineralic and polymineralic aggregates with varying subgrain sizes, volatile-rich and volatile-poor compositions, most at approximately 6 km s^{-1} (appropriate for simulation of the Stardust Wild 2 encounter). This provides a visual key to impacts by known materials, whose properties can subsequently be studied at fine scale. We extend the discussions of Burchell et al. (2008a) and Price et al. (2010), evaluate the roles of impactor density and internal structure, and explore the importance of aggregate flattening and fragmentation compared with expansion of released volatile components, in the creation of Type B and C tracks.

EXPERIMENTAL METHODS AND MATERIALS

Aerogel Targets

The aerogel targets came from a range of sources, and were used opportunistically as supplies became available. Dense aerogel (60 kg m^{-3} and above) came from Matsushita Electronics Works, Japan. Lower density aerogel blocks came from Chiba in Japan (see Okudaira et al. 2004) or were manufactured in house at Kent (Foster 2006; Burchell et al. 2009a). Peter Tsou and Steve Jones of the Jet Propulsion Laboratory supplied two types of graded aerogel similar to that flown on Stardust: from Peter Tsou came “flight spare” Stardust aerogel (FSSA, manufactured as described in Tsou et al. 2003; and as used in Burchell et al. 2008a); the new aerogel samples used in later shots were manufactured by the same method, and are referred to as “flight-quality” Stardust aerogel (FQSA, see Jones [2007] for details of their manufacture). To be able to make a reliable comparison of track morphology between differing projectile types, especially the measured ratios of stylus and bulb dimensions, it is very important to utilize targets with similar properties, especially density, as this plays a major role in the track formation process

(Burchell et al. 2009a). In this publication, although we illustrate and describe some tracks in both lower and higher density targets, we will concentrate our discussion and interpretation on only a subset of our experimental data, i.e., tracks created in aerogel of approximately 30 kg m^{-3} density ($30 \pm 2.4 \text{ mg cm}^{-3}$), intermediate between the surface and deep density in Stardust collector aerogel blocks (Burchell et al. 2009a). Comparison of tracks made by the same projectiles and velocity impacted together, simultaneously, onto both constant density ($30 \pm 2.4 \text{ mg cm}^{-3}$) and “flight-quality” Stardust-graded aerogel, show that track shape is not significantly different between the two targets, although the overall track size may be a little larger in our constant density aerogel blocks (see Fig. 4f). Previous studies of the alteration of impacting particle properties (e.g., Fries et al. 2009) have also shown that the thermal response of delicate impactors shot into this approximately 30 kg m^{-3} aerogel is similar to that in graded “flight spare” Stardust aerogel. We therefore suggest that our targets provide an acceptable comparison for the fate of an impactor penetrating more than a few millimeters deep into graded aerogel, and hence also the response of aerogel to the particular impactor type. We do, however, note that very short tracks seen in the aerogel collector on Stardust are confined to a very low density surface portion of the block, and even if made by an aggregate particle, their shape may reflect a lower degree of particle modification during capture.

Projectile Materials

All were fired as sabot-filling “buckshot” powders at approximately $5\text{--}6 \text{ km s}^{-1}$ in the LGG at the University of Kent in Canterbury, using the protocol of Burchell et al. (1999). This well-established technique produces large numbers of impacts upon a relatively small area, ideal for conserving limited supplies of target materials (such as low density aerogel). Almost every shot employed only a single projectile type in the sabot, or two materials of very different grain size and properties (e.g., large soda-lime glass and much smaller polystyrene beads), whose tracks could be distinguished easily. One shot (G130411#1) used a mixed mineral powder (cronstedtite, enstatite, diopside, Ca-feldspar, and pentlandite), with tracks made by cronstedtite and the feldspar subsequently being identified by Raman spectroscopy of terminal particles.

Most of the projectile powders came from the same samples and batches as prepared for impact preservation experiments on Stardust aluminum foils (Kearsley et al. 2006, 2007, 2008; Wozniakiewicz et al. 2011), the robust mineral powders having been prepared in a pestle and

mortar, then separated into size fractions by calibrated sieves. The coarsest fraction (>250 micrometers) was usually removed, leaving only finer particles for use, as their track length would be unlikely to exceed the dimensions of available aerogel targets. Although our projectiles were chosen to have appropriate composition for cometary dust analogs, we did not set out to determine a precise size calibration for each projectile type. Indeed, their nonspherical grain shapes (Fig. 2) make them difficult to compare with previous, simple calibration projectiles. Evidence from penetration-hole size distribution in earlier thin polymer foil impact experiments (e.g., Kearsley et al. 2005) showed that fragmentation (probably along internal planes of weakness) during experimental acceleration may also change both size and shape in some impactor types, complicating the relationship between the sieve size fraction determined before the shot, the actual grain size on impact, and the resulting dimensions of the aerogel tracks.

Where necessary, new samples were purchased, to be added to the mineral projectile suite at the Natural History Museum (NHM) in London. All were characterized and confirmed by energy dispersive X-ray (EDX) microanalysis prior to use, but these later samples are not yet added to the cataloged collection at NHM. A range of organic materials were purchased for investigation of Al foil cratering (Kearsley et al. 2010), and their polydisperse powders were then used for aerogel shots. Pristine samples of all the prepared projectiles used in this study have been retained at NHM for further analysis as necessary. Representative samples from the projectile powders are illustrated in the scanning electron microscope (SEM) images of Figs. 2 and 3, with details of each shot given in Table 1.

In this study, we describe impacts by organic particles which contain components with low melting and dissociation temperatures ($<250^\circ\text{C}$), from which volatile gases may be expelled during and following heating by impact. In the future, tracing the evolution and dispersal of gaseous fractions from these materials will be useful for understanding the capture and modification of cometary organic matter, extending the study by Fries et al. (2009). In the current paper, we do not specifically consider impacts on aerogel by particles that are made of highly volatile materials such as ices. Water ice was considered unlikely to be present within the dust sampled by Stardust (Burchell and Kearsley 2009), as liable to sublimation within the coma (Beer et al. 2006), during relatively long exposure of the particles before intersecting the path of the spacecraft (Sekanina et al. 2004). However, detectable water ice has been reported within the coma of other comets at relatively long heliocentric distance (Kawakita et al.

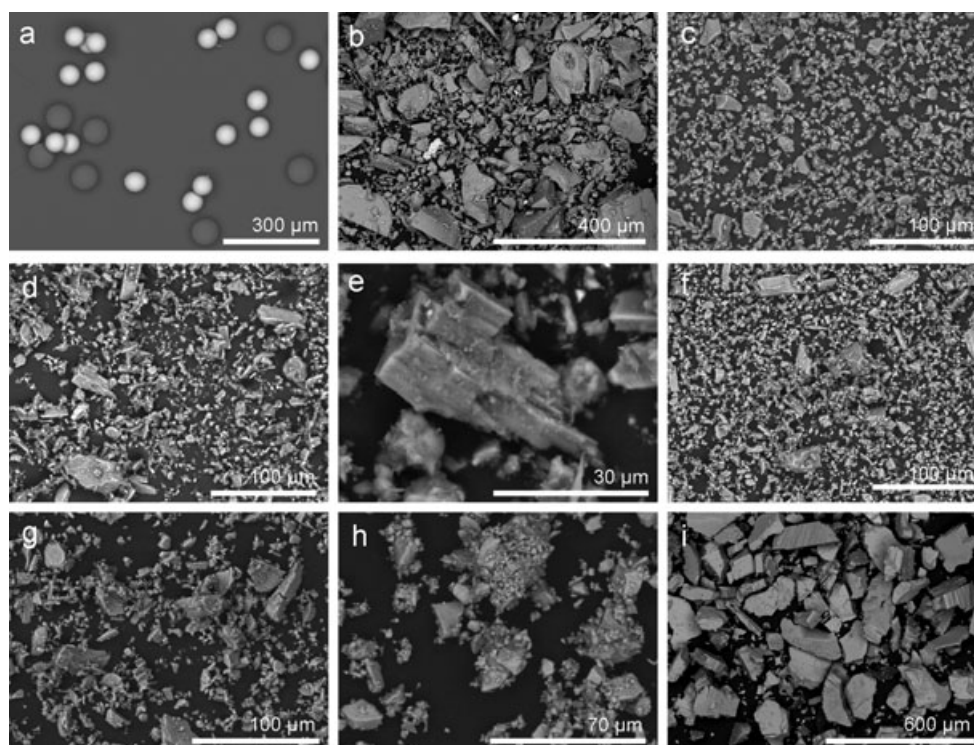


Fig. 2. Projectile materials. a) Backscattered electron image of 63.51 μm monodisperse soda-lime glass spheres (bright) mixed with 79.55 μm monodisperse PMMA spheres (darker). b) Basalt glass powder, USGS NKT-1G. c) Olivine powder from Admire pallasite meteorite (BM1950-337). d) Enstatite orthopyroxene powder (BM.2005,M318). e) Higher magnification view shows cleavage planes in enstatite orthopyroxene grain. f) Diopside clinopyroxene powder (BM.2005,M310). g) Ca-rich feldspar (An approximately 84) (BM.2005,M312). h) Pyrrhotite iron sulfide (BM.2005,M317), clumped fine fraction, as used in aggregates. i) Cronstedtite hydrous Fe silicate, NHM.

2004), and even close to 1 AU (A'Hearn et al. 2011), and we are therefore attempting experimental impacts by water (and other) ices. Most of the technical difficulties of launching solid water ice projectiles in the LGG have now been overcome, and their impact craters with distinctive surface textures on foil have been reported (Burchell et al. 2011). No craters of this type have yet been reported amongst the many hundreds examined on Stardust foils, supporting the suggestion that little ice was encountered. Broad dispersion of ice fragments occurs during LGG shots, making successful impact on a small aerogel target (as opposed to a large foil area) less certain. Nevertheless, when sufficient aerogel target material becomes available, this will be investigated further.

Monomineralic, Single Grain Mineral Projectiles

For grain-preservation and analysis protocol experiments prior to the return of Stardust, polydisperse projectile materials were chosen to represent the most abundant mineral phases expected to be found in comet Wild 2: Mg-rich olivine, Mg-rich orthopyroxene, Ca and Mg-rich clinopyroxene, Ca-rich feldspar; alkali-rich and

mafic-rich amorphous materials (glasses); Fe sulfide (pyrrhotite). These have subsequently been confirmed as abundant components in the Stardust collection, with the mafic silicates and sulfide being a good match with the bulk of the assemblage reported by Zolensky et al. (2006, 2008). In addition, two hydrous silicates (lizardite Mg-serpentine, and the Fe-silicate cronstedtite) were shot, as similar materials might have been expected in Stardust samples had there been substantial aqueous parent body processing on the comet Wild 2 nucleus. Alteration of these two minerals during hypervelocity capture in aerogel has also been described by Okudaira et al. (2004, 2005) and Noguchi et al. (2007), but the preimpact morphology of their projectiles was not described, and little information was given as to track shape.

Noncrystalline Anhydrous Silicates (Glasses)

We utilized two types of glass. Soda-lime glass spheres (Fig. 2a) were supplied as monodisperse size calibration standards by Whitehouse Scientific plc, UK, (<http://www.whitehousescientific.com/>), being the same samples used in both the earlier Type A aerogel track calibration (Burchell et al. 2008a) and the larger aluminum crater size calibration of Kearsley et al.

Table 1. Impacts on silica aerogel: of constant density, or graded (Flight Spare Stardust Aerogel, FSSA or Flight Quality Stardust Aerogel, FQSA), using the LGG at Canterbury, bold type denotes illustrations and data from this particular experiment are presented and discussed in this publication. Projectile grain size was controlled by sieving through a mesh of “Pass” value in μm . Maximum (Max) and minimum (Min) grain dimension values were determined by SEM of subsamples. Note that the long axis Max may exceed “Pass” where narrow, elongate grains passed through the sieve. Pyrrhotite grain size (marked †) reflects clumping, individual grains may be smaller. Materials marked with an asterisk (*) are likely to fragment during LGG acceleration, and their size distribution will therefore probably skew to a smaller size before impact at target.

Projectiles	Projectile density (g cm^{-3})	Projectile grain size (μm)	Shot number	Vel. km s^{-1}	Aerogel density (kg m^{-3})
Soda-lime glass beads (monodisperse)	2.37 ^a	50 103 63.51 \pm 1.78 63.51 \pm 1.78	G130508#2 G201004#1 G151211#1 G151211#1	6.11 5.18 6.40 6.40	33 30 30 FQSA
Basalt glass NKT-1G (polydisperse)	$\sim 2.8^a$	Pass 250 Max 180 Min < 5	G130111#1 G051206#2 G110505#2	6.41 5.88 6.10	FSSA 25 16–19
Olivine (Fo ~ 88) (polydisperse)	3.36 ^b	Pass 20 Max > 25 Min < 2	G211106#2	5.89	30
Enstatite (En ~ 95) (polydisperse)	3.2 ^b	Pass 38 Max > 56 Min < 2	G220206#2	5.86	~ 60
Diopside (En 36:Fs15:Wo49) (polydisperse)	3.36 ^b	Pass 38 Max > 55 Min < 2	G270400#3 G150206#3	5.10 5.84	30 30
Feldspar (An ~ 84) (polydisperse)	2.72 ^b	Pass 38 Max > 48 Min < 2	G130411#1 G091205#2	6.12 5.92	~ 30 60
Pyrrhotite (polydisperse)	4.63 ^b	Pass 53† Pass 53†	G290409#1 G290409#2	6.39 5.89	31 FSSA
Cronstedtite (polydisperse)	3.3 ^c	Pass 250* Max > 280 Min < 10	G130411#1	6.12	~ 30
Lizardite (aggregate) (polydisperse)	$\sim 2.5^b$	53–125* > 125* > 125*	G021205#1 G310505#2 G110205#3	5.96 5.04 5.00	30 60 60
Allende powder (polydisperse)	2.79 bulk ^d 3.30 grain ^d	Pass 125 Max > 145 Min < 2	G140507#4	5.91	26
Murchison powder (polydisperse)	2.25 bulk ^d 2.90 grain ^d	Pass 250 Max > 280 Min < 5 53–125 < 500*	G042105#3 G151006#1 G140507#1 G140507#3	4.93 5.81 6.11 6.21	60 30 30 30
Orgeuil powder (polydisperse)	1.60 bulk ^d 2.46 grain ^d	< 500*	G120709#1 G210709#2	6.02 6.18	~ 30
fine diopside, coarse pyrrhotite; acrylate (polydisperse)	~ 3 bulk ^e	< 500*	G221208#2	6.08	FSSA
Olivine, diopside + pyrrhotite aggregates (polydisperse)	~ 2.4 bulk ^e	< 500*	G300709#2	6.09	~ 30
olivine, SiC, TiC, Si ₃ N ₄ , TiN, Al ₂ O ₃ + diamond aggregates (polydisperse)	~ 2.4 bulk ^e	< 500*	G210110#3	6.42	27
Acrylic Fixative (polydisperse)	$\sim 1.2^f$	< 20*	G281009#1 G151211#1 G151211#1	6.28 6.40 6.40	32 30 FQSA
Poly methylmethacrylate (monodisperse)	1.19 ^f	31.62 \pm 1.56 79.55 \pm 1.79 79.55 \pm 1.79			

Table 1. *Continued.* Impacts on silica aerogel: of constant density, or graded (Flight Spare Stardust Aerogel, FSSA or Flight Quality Stardust Aerogel, FQSA), using the LGG at Canterbury, bold type denotes illustrations and data from this particular experiment are presented and discussed in this publication. Projectile grain size was controlled by sieving through a mesh of “Pass” value in μm . Maximum (Max) and minimum (Min) grain dimension values were determined by SEM of subsamples. Note that the long axis Max may exceed “Pass” where narrow, elongate grains passed through the sieve. Pyrrhotite grain size (marked †) reflects clumping, individual grains may be smaller. Materials marked with an asterisk (*) are likely to fragment during LGG acceleration, and their size distribution will therefore probably skew to a smaller size before impact at target.

Projectiles	Projectile density (g cm^{-3})	Projectile grain size (μm)	Shot number	Vel. km s^{-1}	Aerogel density (kg m^{-3})
Poly oxymethylene (polydisperse)	1.43 ^a	< 500	G191109#3	5.90	~ 30
Glycine (polydisperse)	1.16 ^a	< 500	G011009#3	6.06	~ 30
¹⁵ N doped Urea (polydisperse)	~1.4 ^a	< 500	G191109#2	6.04	~ 30
Coal PSOC 1534	~1.3 ^g	< 500*	G040108#1	6.22	31
Sub-bituminous (polydisperse)					
Coal PSOC 1468	1.6 ^h	< 180	G261108#1	6.13	FSSA
Anthracite (polydisperse)					
Graphite (polydisperse)	~2.4 ^f	< 500*	G191207#2	6.33	32

Representative projectile density values are taken from: ^asuppliers' literature; ^bDeer et al. (1992); ^c<http://webmineral.com/data/cronstedtite.shtml>;

^dConsolmagno et al. (2008) for bulk meteorites (including porosity) and grains (solid, with no porosity); ^ecalculated from mineral, pore-space, and adhesive proportions measured in SEM images and EDX maps of polished sections (Kearsley et al. 2009); ^fLide (2008); ^gAtria et al. (1994);

^hSpeight (2005, p. 115, Fig. 6.1).

(2006). These beads have a narrow shape and size range and uniform composition (hence constant density), thereby constraining three important variables that might control aerogel track dimensions. They are solid; lack porosity, fractures, or crystallographic cleavage planes; and have proven to be robust during LGG shots, the majority reaching the target as intact spheres, although significant ablation and fracturing may occur during track formation (Burchell et al. 2009a).

Basalt glass powder (Fig. 2b) was prepared by crushing a small sample of United States Geological Survey NKT-1G standard. The same projectile sample was used in Kearsley et al. (2006) and Marcus et al. (2008). The particles are both polydisperse and angular, often curved, although not markedly inequant. They are homogeneous in composition and density, and lack internal pore space or crystallographic cleavage.

Crystalline Anhydrous Silicate Mineral Powders

Olivine powder (Fig. 2c) was prepared from isolated clean grains of the Admire pallasite meteorite (BM1950-337); Enstatite powder (Figs. 2d and 2e) from BM.2005,M318 (an ultrabasic rock from Ødegården Mine, Bamble, Norway); Diopside powder (Fig. 2f) from BM.2005,M310 (a single large crystal, collected from Yates Mine, Sandy Creek, Otter Lake, Quebec, Canada); Ca-feldspar powder (Fig. 2g) determined by electron microprobe as An approximately 84:Ab approximately 16, from BM.2005,312 (large crystals within partially retrogressed granulite facies anorthositic gneiss, from

Majorqap qava, Fiskenaesset, S.W. Greenland). These powders are all polydisperse and angular materials. The olivine shows an equant grain shape (reflecting poor crystallographic cleavage, Deer et al. 1992); whilst the enstatite, diopside, and the feldspar have more inequant grains, with the pyroxenes showing the presence of two good crystallographic cleavage planes (e.g., Fig. 2e).

Crystalline Sulfide Mineral Powders

Pyrrhotite powder (Fig. 2h) was prepared from BM.2005,M317 (a hand-specimen from Drag, Tysfjord, Nordland, Norway). The powder is polydisperse, angular, and equant, tending to clump due to strong magnetism, but apparently separating into individual grains during LGG acceleration. The same projectile sample was used in the study of sulfide capture by aerogel reported by Ishii et al. (2008), and the preservation of sulfide remnants in foil craters by Kearsley et al. (2007) and Wozniakiewicz et al. (2011, 2012).

Crystalline Hydrated Silicate Mineral Powders

Cronstedtite powder (Fig. 2i) was prepared by crushing a fibrous botryoidal vug-lining from an uncataloged but characterized sample at the NHM. This hydrated layer silicate is a member of the kaolinite-serpentine groups and has an ideal stoichiometric formula of $\text{Fe}^{2+}_2\text{Fe}^{3+}(\text{SiFe}^{3+})\text{O}_5(\text{OH})_4$. The projectile powder was left at a relatively coarse grain size as it was expected it would break up into acicular shards during flight. Individual projectile grains are solid, lacking pore

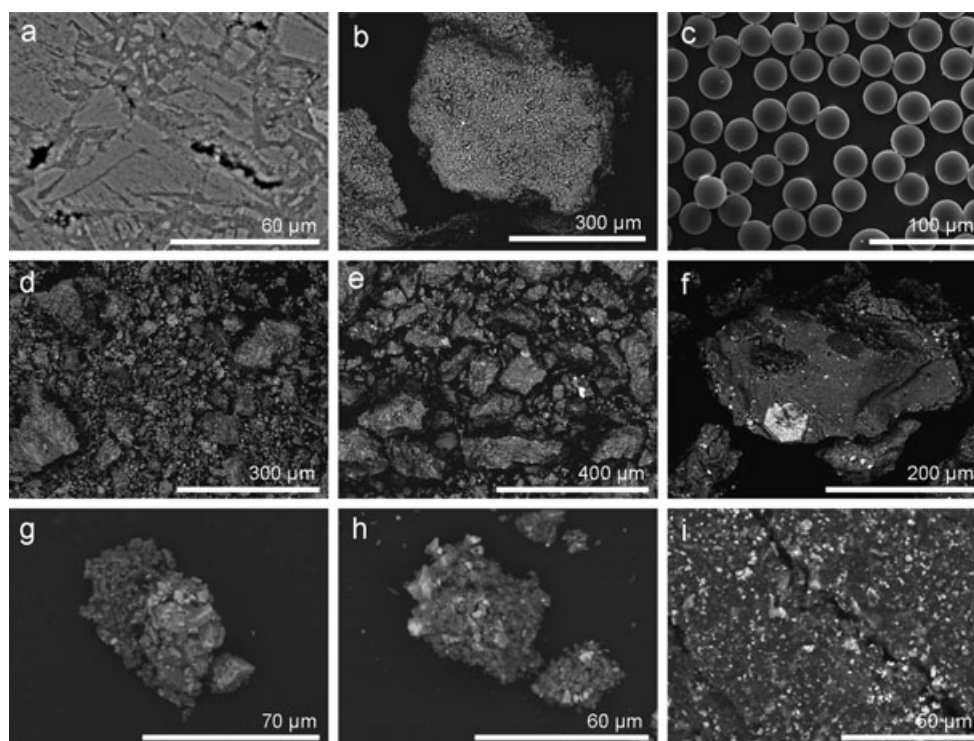


Fig. 3. Projectile materials (Continued) a) lizardite, polished section showing complex internal subgrains in this natural aggregate, BM43217; b) lizardite projectile, BM43217; c) poly methylmethacrylate monodisperse spheres; d) Allende CV3 carbonaceous chondrite meteorite powder e) Murchison CM2 carbonaceous chondrite meteorite powder (BM.1988.M23); f) Orgueil CI1 carbonaceous chondrite meteorite powder, note the large euhedral iron sulfide grain; g) artificial aggregate of fine diopside mixed with coarser pyrrhotite powder; h) artificial aggregate of fine diopside, olivine, and pyrrhotite powder; i) artificial presolar grain aggregate cake, prior to breakage into separate projectile grains.

space. Like lizardite, they have a single perfect $\{001\}$ crystallographic cleavage.

Lizardite serpentine (Fig. 3b) powder was prepared by crushing grains of BM43217 (a thick vein sample from the Lizard, Cornwall). This almost monomineralic serpentine (with a very small quantity of talc) is hard but porous, made of randomly oriented, clustered stacks of fine hydrated silicate plates (Fig. 3a), forming a natural aggregate. It is the same projectile material which made the single lizardite aerogel track illustrated by Burchell et al. (2008a) and the foil craters in fig. 22 of Kearsley et al. (2008).

Natural and Artificial Polymineralic Aggregate Projectiles

From analyses of the Stardust aluminum foils (Hörz et al. 2006; Kearsley et al. 2008; Price et al. 2010) and many particles extracted from aerogel (Brownlee et al. 2006; Zolensky et al. 2008), it is clear that polymineralic aggregates rather than monomineralic, monocrystalline grain impactors dominate the Wild 2 dust. To simulate impacts by such polymineralic grains, a range of natural and, later, artificial aggregates were prepared, as detailed below.

Meteorite Powders

Natural aggregate projectiles were produced by crushing small quantities from three meteorites, previously used for Raman spectroscopy of particles captured in aerogel (Burchell et al. 2006b). In each case, when examined by backscattered electron imagery, the powder was seen to contain a wide range of particle sizes, with many individual grains containing a combination of minerals, typical of their specific assemblages as described in Brearley and Jones (1998). The projectiles were thus polydisperse, being a mixture of coarser, crystalline monomineralic grains, and fine-grained polymineralic aggregates. Their resistance to preparation by crushing revealed that all three meteorites are relatively strong, and their aggregate projectiles are likely to be fairly robust, rather than very weak.

Allende (CV3 carbonaceous chondrite) powder (Fig. 3d) was made from an uncataloged but characterized sample at NHM. The powder shows diverse compositions and structures within polydisperse grains, many being fine-grained and rather porous aggregates dominated by Fe-rich olivine (probably comminuted matrix), with larger (approximately 50 μm) angular but equant grains that are almost monomineralic Mg-rich olivine and orthopyroxene,

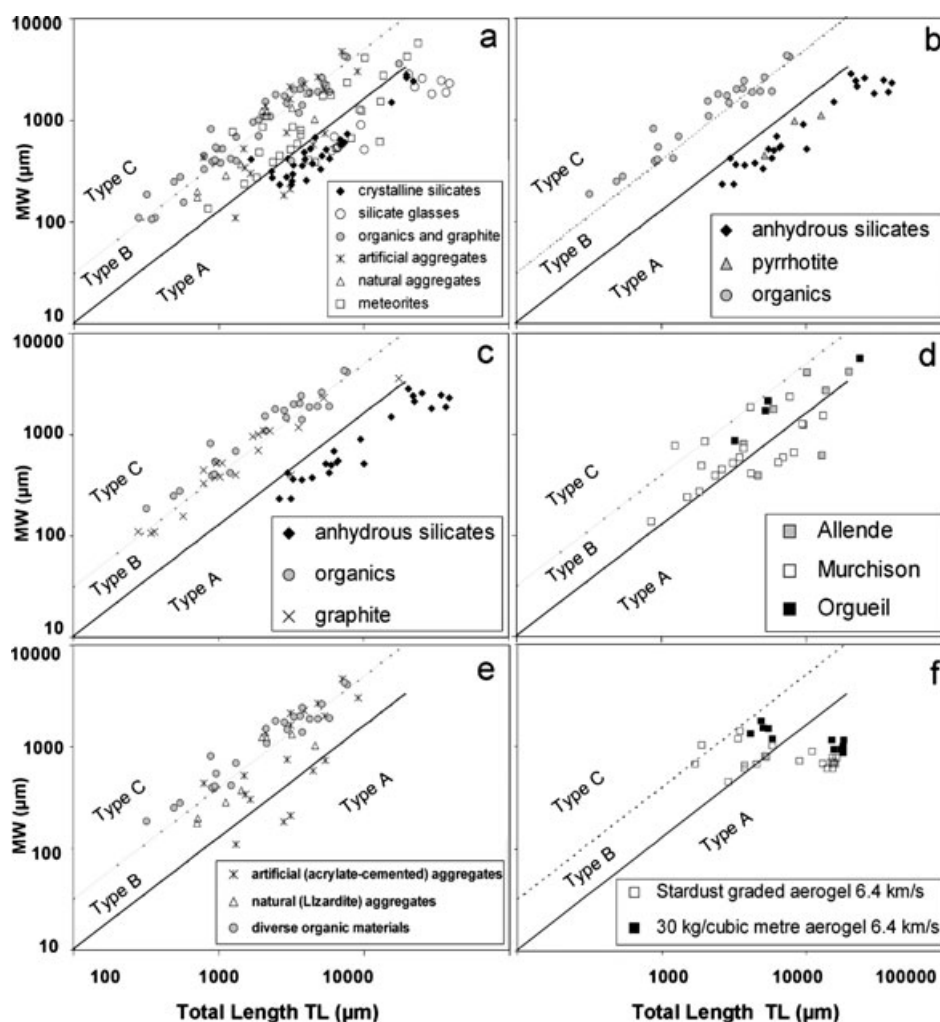


Fig. 4. a–e: Summary of results: plots of maximum width (MW) versus total length (TL) for tracks in aerogel of approximately 30 kg m^{-3} density, made by LGG shots of particles listed in Table 2. Boundary lines between track types A–B and B–C are the same as those derived for Stardust Wild 2 dust tracks by Burchell et al. (2008a). The natural aggregate projectiles in (a) were made by crushing porous lizardite serpentine; f) comparison of tracks made by $63.51 \mu\text{m}$ soda-lime glass and $79.55 \mu\text{m}$ PMMA spheres impacting two aerogel samples: Stardust (FQSA, graded from 5 kg m^{-3} at surface to 50 kg m^{-3} at depth); and uniform approximately 30 kg m^{-3} .

with variable Fe-content (probably broken chondrule fragments). A wide diversity of minor components include alkali-bearing aluminosilicate with calcic clinopyroxene (probably chondrule mesostasis), spinel and clinopyroxene with nepheline and sodalite (fragments of altered calcium-aluminum-rich inclusions) and small Fe-rich sulfides, oxides, and Ni-rich metal. No evidence was seen of abundant hydrous silicates, but the high porosity (approximately 23%, Consolmagno et al. 2008) is evident.

Murchison (CM2 carbonaceous chondrite) powder (Fig. 3e) was prepared from a subsample of BM1988.M23. The majority of the polydisperse projectile particles contain very fine subgrains (reflecting the high sub- μm matrix content of this meteorite) and are polymineralic, with only a few larger Mg-rich olivine

and orthopyroxene grains (sparse chondrule fragments and isolated matrix grains), together with occasional Fe-sulfide and Ca-carbonates. The matrix is known to contain substantial hydrated silicate and aluminosilicate phases (see Brearley and Jones 1998). The high bulk porosity (approximately 22%, Consolmagno et al. 2008) is not apparent in SEM images.

Orgueil (CI1 carbonaceous chondrite) powder (Fig. 3f) was prepared from an uncatalogued but characterized sample at NHM. This powder is polydisperse and polymineralic, most subgrain constituents being extremely fine-grained (sub μm) of complex silicate and sulfide mixed composition, probably reflecting the abundant hydrated interlayered phyllosilicates in CI groundmass (see discussion in Brearley and Jones 1998).

Micrometer-scale Fe oxide is abundant, as are euhedral Fe sulfides, including coarser grains up to approximately 60 μm (Fig. 3f). Occasional Ca-carbonate/phosphate grains are also present. Fine porosity is not visible in our SEM images (and is suggested to be low by Corrigan et al. 1997). However, it is likely that some individual powder grains may have been weakened by the rapid internal growth of hygroscopic sulfate minerals (Gounelle and Zolensky 2001), leading to much higher internal porosity, such as reported by Consolmagno et al. (2008).

Fine-Grained Artificial Mineral Aggregates

Aggregates were prepared using a modified protocol similar to Kearsley et al. (2009). The very finest grain size silicate components of the aggregate particles were prepared by milling in a TEMA Machines Ltd vibratory mill, followed by timed aqueous column sedimentation to remove grains $>4\ \mu\text{m}$, and drying of the supernatant suspension to produce “monodisperse” powders of less than 4 μm grain size for olivine and diopside. Olivine grains were hand-picked from an ultrabasic nodule in basalt from the San Carlos Reservation, Arizona; and diopside from BM.2005,M310 (Yates Mine, Quebec).

A powerful magnet was used to pull fine pyrrhotite powder (from an uncataloged NHM sample from Russia) through micropore filters, creating fractions of $<10\ \mu\text{m}$ and $<20\ \mu\text{m}$ (Fig. 1h), although both showed a tendency to later aggregate into clusters, resulting in uneven mixing within aggregate powders (e.g., Fig. 10f).

The dry powders were made into a slurry in distilled water, then mixed together (as appropriate) to form a range of aggregate types. Each mixture was dried in a watch-glass, then spray impregnated with Winsor and Newton Pastel Fixative (a proprietary acrylic formulation). Evaporation of the solvents on a hot plate allowed the mixture to harden as aggregate “cake.” In all the examples shown in this article, the intermineral pore space was effectively completely filled by acrylic of approximately $1\ \text{g cm}^{-3}$ density. Samples were then scraped from the watch-glass using a clean stainless steel scalpel blade, yielding relatively weak cake fragments of up to millimeter scale, for use as projectiles. From results of our previous shots onto Al foil (Kearsley et al. 2009), it is apparent that the cake breaks up during LGG acceleration, giving a range of impactor sizes at the target, from individual subgrains (4 μm and less) up to aggregates containing many component subgrains, and reaching over 100 μm overall diameter.

Three types of artificial aggregate particles are illustrated in this paper:

1. “Polydisperse” aggregates (Figs. 3g and 10e); made from diopside ($<4\ \mu\text{m}$), and pyrrhotite ($>20\ \mu\text{m}$), cemented by acrylic.
2. “Monodisperse” aggregates (Figs. 3h and 10f); made from olivine and diopside (both $<4\ \mu\text{m}$); and pyrrhotite ($<10\ \mu\text{m}$), cemented by acrylic.
3. Presolar grain simulant aggregates (Fig. 3i); composed of olivine ($<8\ \mu\text{m}$), with small quantities of diamond (approximately 1 μm), alumina (approximately 1 μm), Si carbide (approximately 6 μm), Si nitride ($<3\ \mu\text{m}$), Ti carbide ($<4\ \mu\text{m}$), and Ti nitride ($<3\ \mu\text{m}$), cemented by acrylic.

Organic Projectiles

Pure Synthetic Organic Materials

These samples were purchased to investigate crater morphology and preservation of foil impact residues (Kearsley et al. 2010). The most widely used organic material in our shots onto aerogel was the Winsor and Newton Pastel Acrylic Fixative described above, used to cement our mineral aggregates. A separate clean sample of this acrylic compound, without mineral grains, was prepared as a thick spray layer on a watch glass, dried on a hotplate (approximately 120 $^{\circ}\text{C}$), then scraped as loose shards for use as projectiles.

Monodisperse poly methylmethacrylate (PMMA) spheres of 30 μm diameter (Fig. 3c) were supplied by S. Armes (U. Sheffield, UK), and 80 μm monodisperse spheres (Fig. 2a) were taken from the same batch used in Burchell et al. (2004), and in studies of crater size dependence upon projectile density (Kearsley et al. 2007).

Glycine powder was purchased from Sigma Aldrich (catalogue number 410225), and used for both foil (Kearsley et al. 2010) and aerogel shots (see Nixon et al. 2012).

Urea was crystallized from a ^{15}N -labeled sample (supplied by CDN isotopes, catalogue number N-2449) mixed in aqueous solution with urea of normal terrestrial light element stable isotope ratios. The dried crystalline powder was dense and polydisperse.

Poly oxymethylene (POM) polydisperse powder was prepared by filing of a large polymer block purchased from Goodfellow (catalogue number 881-467-82). This polymer was chosen as it has been postulated as present in cometary dust by Cottin et al. (2004).

Coal Samples

Well-characterized coal samples were purchased from the U.S. Department of Energy Coal Sample (DECS) Bank and Database for a study of impact-driven alteration during particle capture in aerogel, described by Fries et al. (2009). For the present study, we examined tracks from two different types of coal to document the possible variation in track formation behavior between impactors with varying composition (especially oxygen

content). The following sample descriptions are based on data from the DECS website (<http://www.energy.psu.edu/copl/doesb.html>).

The sub-bituminous coal sample number PSOC 1534 (Waterfall seam) contains approximately 63% carbon, has a high O/C atomic proportion (0.32), with lesser hydrogen and nitrogen, sulfur below detection limit, and nonorganic mineral matter (ash) determined as 11.1% by weight. Analytical SEM revealed a small quantity of kaolinitic clay. The anthracite coal sample number PSOC 1468 (Buck Mountain seam) contains 89% carbon; approximately low O/C (0.02); very small quantities of hydrogen, nitrogen, and sulfur; and ash determined as 6.8% by weight. Porosity of such anthracites is typically very low (1.3%, Atria et al. 1994). For further description of these coals, and their impact-driven alteration, see Fries et al. (2009).

Graphite Powder

This is the same sample described by Fries et al. (2009), obtained as a commercially supplied graphite powder, and is effectively 100% pure carbon, of high crystallinity. SEM of a subsample from the projectile grains shows them to be platy clusters of $<30\text{ }\mu\text{m}$ diameter.

Imaging

Tracks in impacted aerogel targets were photographed on a glass or transparent plastic surface, with side or back lighting, using Canon and Nikon macrophotographic cameras at NHM; and on a Wild stereo microscope with Nikon 995 Coolpix camera in macro mode, also at NHM. Images were converted to grayscale, brightness and contrast were enhanced, and side-lit images were processed to give a negative gray scale for clarity of detail (e.g., Figs. 10g and 10h). As it is common to find surface darkening of aerogel targets after light-gas gun shots, it was necessary to slightly tilt some targets, to see proximal portion of tracks (e.g., Figs. 5h–j). In some cases, although the main track shape was clearly apparent, subtle irregularity of the target surface and a fine coating of gun-derived dark soot prevented imaging of the portion of the track at, and immediately below, the entrance hole (e.g., Fig. 5a). For the figures within this article, the contrast and brightness of the upper parts of such tracks were adjusted. The illustrated tracks, which appear to be nonperpendicular to the aerogel surface, also reflect the gently undulating surface of the target. The projectile powders, and examples of the enstatite and lizardite impact tracks, were imaged by (SEM) using JEOL 5900LV, LEO 1455VP and Zeiss EVO 15 LS instruments equipped with Oxford Instruments energy dispersive X-ray (EDX)

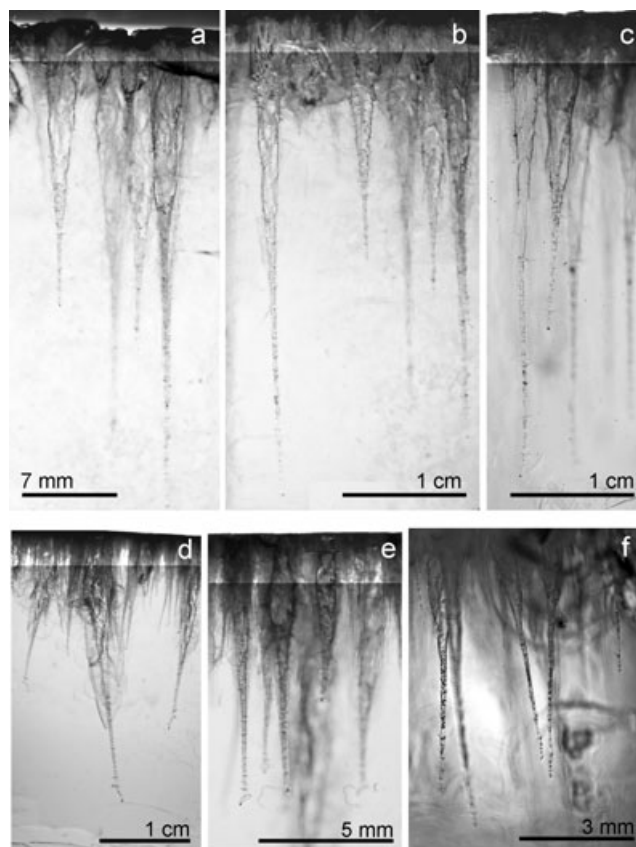


Fig. 5. Tracks of Type A created by impacts of: a–c) soda-lime glass beads, shot G201004#1 impacted at 5.18 km s^{-1} ; d–f) polydisperse basalt glass powder shot G130111#1 at 6.41 km s^{-1} into Stardust-graded aerogel. Note adjusted brightness and contrast for upper part of track images, to compensate for a dark aerogel surface.

microanalysers, running INCA software. The tracks produced by the monodisperse polymineralic aggregate shot were imaged by X-ray Micro-Computed Tomography using the X-Tek (Nikon Metrology) HMX-ST CT at NHM, with false color and stereo anaglyph rendering through 3D Studio MAX.

Experimental Results

Noncrystalline Silicates (Glasses)

Both soda-lime glass (Figs. 5a–c), and basalt glass (Figs. 5d–f) created simple, long tapering aerogel tracks of Type A in 30 kg m^{-3} and Stardust-graded aerogel (Figs. 4a and f). All shots of soda-lime glass, using particles from 50 to 105 micrometers diameter, and velocity from just above 5 km s^{-1} to as high as 6.4 km s^{-1} yielded tracks comparable to those of Burchell et al. (2008a), and few showed any division into multiple styli—this is the classic Type A shape. Although not studied as part of this present work, both of these

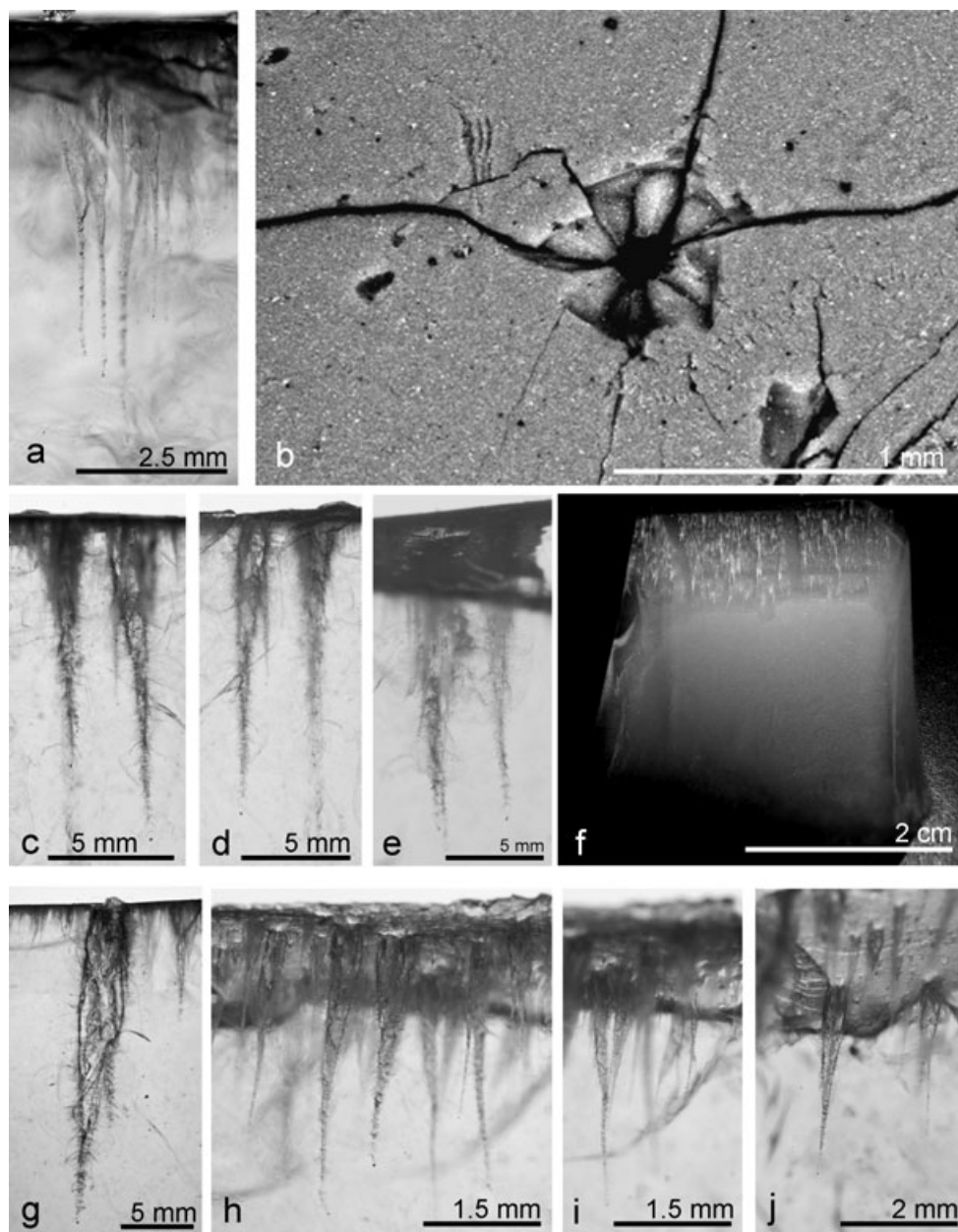


Fig. 6. Tracks of Type A created by impacts of a) Olivine, shot G211106#2; b–f) Enstatite orthopyroxene, shot G220206#2, at 5.86 km s^{-1} , into 60 kg m^{-3} aerogel; g–j) Diopside clinopyroxene, shot G150206#3.

glass materials are known to be affected by impact with aerogel. Soda-lime glass is ablated and the chemical composition of basalt glass is modified (Marcus et al. 2008). Some basalt glass tracks showed visible curvature along their length (Figs. 5d and f).

Crystalline Particles of Anhydrous Silicates

Olivine particles created aerogel tracks of Type A (Fig. 6a). Enstatite orthopyroxene impacted onto higher density aerogel (60 kg m^{-3}) also creates aerogel tracks of

Type A (Figs. 6c–f), with entrance hole and spall zone (Fig. 6b) very similar to the impact of a soda-lime glass sphere shown in fig. 5 of Burchell et al. (2001). Impact into still higher density aerogel (100 kg m^{-3}) produced shorter tracks, with more division into multiple styli and lateral spikes. Diopside clinopyroxene impacts created similar aerogel tracks of Type A, whether impacted onto 30 kg m^{-3} aerogel (Figs. 6g–j), or 60 kg m^{-3} . Ca-rich feldspar (An approximately 84) created aerogel tracks of Type A, but with different maximum width to total

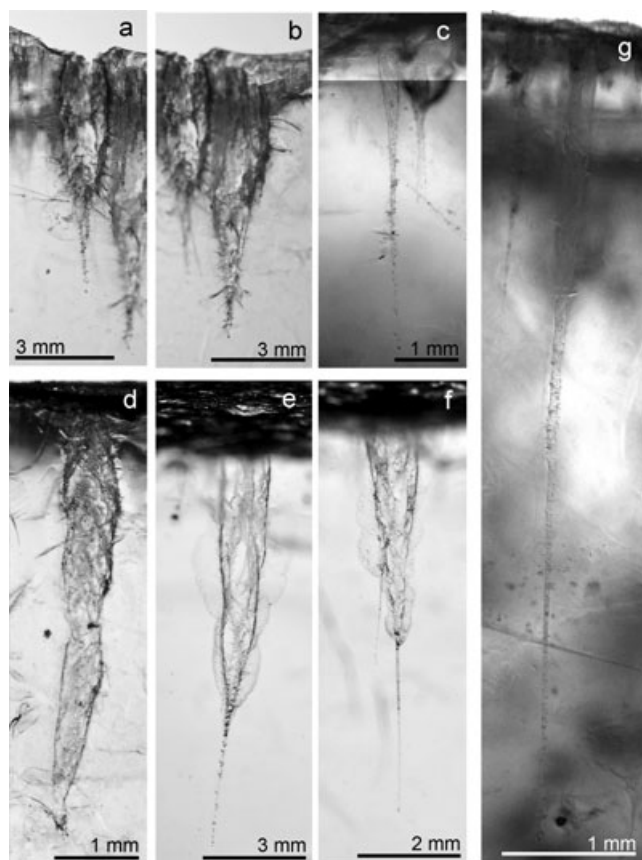


Fig. 7. Aerogel tracks of Type A created by impacts of a–c) Ca-rich feldspar (An approximately 84); a,b) shot G091205#2 (60 kg m^{-3} aerogel); c) shot G130411#1 (approximately 30 kg m^{-3} aerogel); d–f) Pyrrhotite, shot G290409#1; g) Cronstedtite, shot G130411#1.

length ratios, dependent on the target density. Tracks into 30 kg m^{-3} aerogel are long and narrow (Fig. 7c), whereas those into 60 kg m^{-3} are shorter and wider with larger numbers of lateral spikes (Figs. 7a and 7b) of 500 μm to mm length.

Crystalline Sulfides

Pyrrhotite created mainly Type A tracks (Figs. 7d–f) when impacted onto low density silica aerogel under Stardust–Wild 2 encounter conditions. The proximal portion was often surrounded by spiraling fractures (similar to those shown in the tomographic reconstructions of Tsuchiyama et al. 2009), and was rather broader than many of the silicate Type A tracks (as noted by Burchell et al. [2008a] and Ishii et al. [2008]), with an elongate and narrow distal stylus, as noted by Burchell et al. (2008a). In effect, this is a second species of Type A tracks, instead of the classic carrot shape with walls smoothly tapering to the end of the track, there is a shape which resembles the traditional

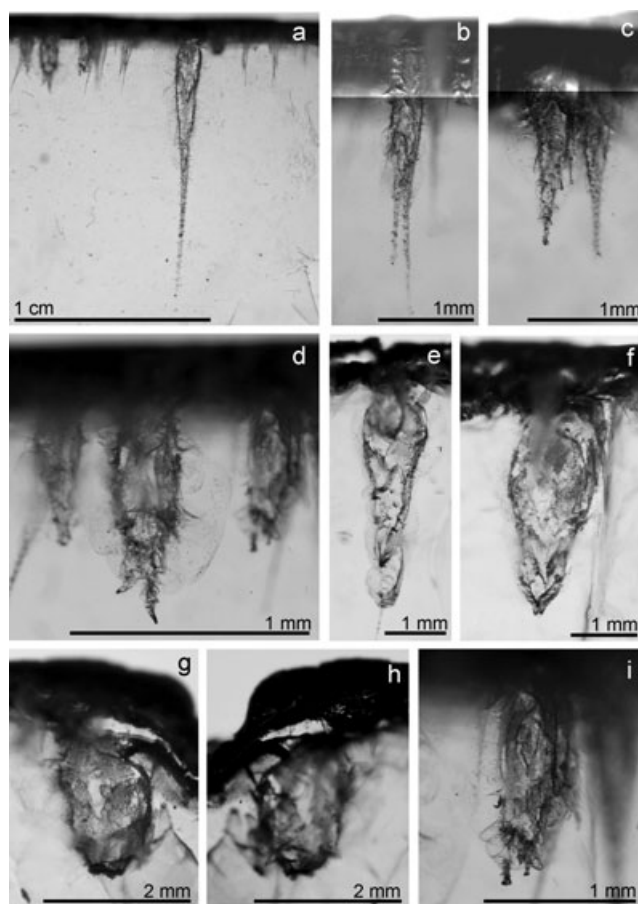


Fig. 8. Aerogel tracks created by impacts of lizardite serpentine powder, showing a wide range of Type A, B (most common) to C. a–c) shot G310505 into 60 kg m^{-3} aerogel at 5.04 km s^{-1} , d–i) shot G021205#1, into 30 kg m^{-3} aerogel at 5.96 km s^{-1} . Brightness and contrast adjusted for upper part of track images, compensating for a dark aerogel surface.

champagne flute glass (with the flat base removed). The bowl is at the start of the track, and the stem leads to the terminal grain.

Crystalline Hydrrous Silicate Impacts

Cronstedtite powder created simple Type A aerogel tracks (Fig. 7g), very similar to those of silicate glass and olivine. However, our lizardite projectiles, which are effectively natural porous aggregates, created a wide range of track types in both 30 and 60 kg m^{-3} aerogel, covering the entire range from rare Type A (Fig. 8a, similar to those of olivine and silicate glasses); through Type B, which were the most common (Figs. 8e and 8f), often with multiple lateral spikes or styli (Figs. 8b–d and i) and small residue fragments located at the tip of the stylus (Fig. 10a) or in the petal-shaped radiating fractures around the bulb (Figs. 10b and 10c); to small bulbous Type C (Figs. 8g and 8h).

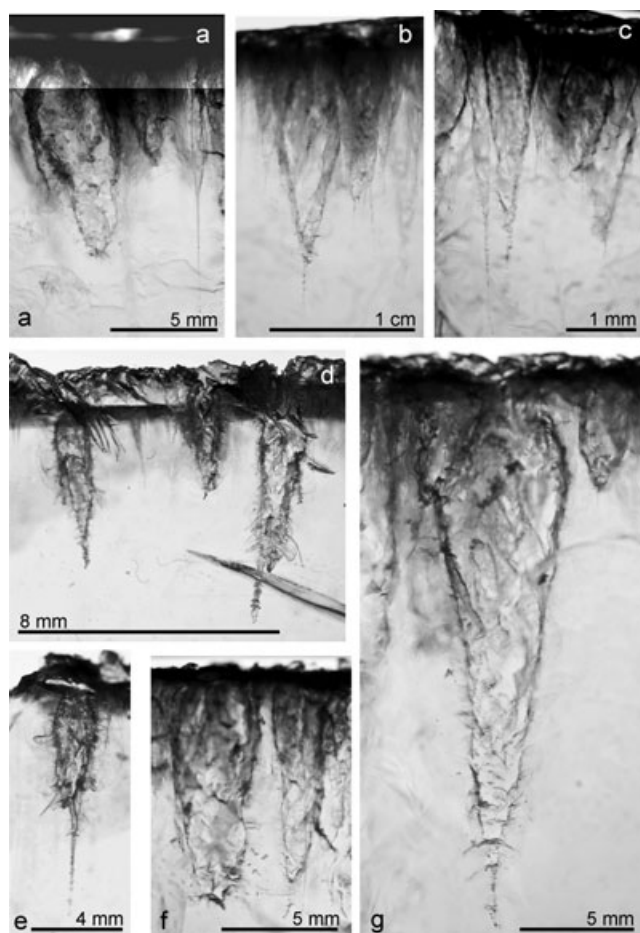


Fig. 9. Aerogel tracks created by powdered meteorites (a–c) Allende, shot G140507#4; d–f) Murchison, shot G042105#3 (g) Orgeuil, shot G140507#3. Brightness and contrast have been adjusted for the upper part of image (a) to compensate for a dark surface.

Meteorite Powders

Allende CV3 powder created numerous larger Type B and smaller Type A tracks, with very variable development of styli (Figs. 9a–c). Murchison CM2 powder also created many Type B tracks with multiple, although usually short, distal styli from the broader portion of the track (Figs. 9d–f) as well as a few Type A tracks, and rare Type C. Orgeuil CI1 powder created a wide range of Type B track shapes, from broad tapering to elongate bulbs (Fig. 9g).

Artificial Aggregate Impacts

Polydisperse aggregates made from fine diopside and coarser pyrrhotite created numerous relatively small Type A tracks and large numbers of Type B, with only a few Type C tracks (Fig. 10d). Monodisperse, fine-grained aggregates of mixed olivine, diopside, and pyrrhotite (Fig. 10f) generated bulbous Type C tracks (Figs. 10g–j),

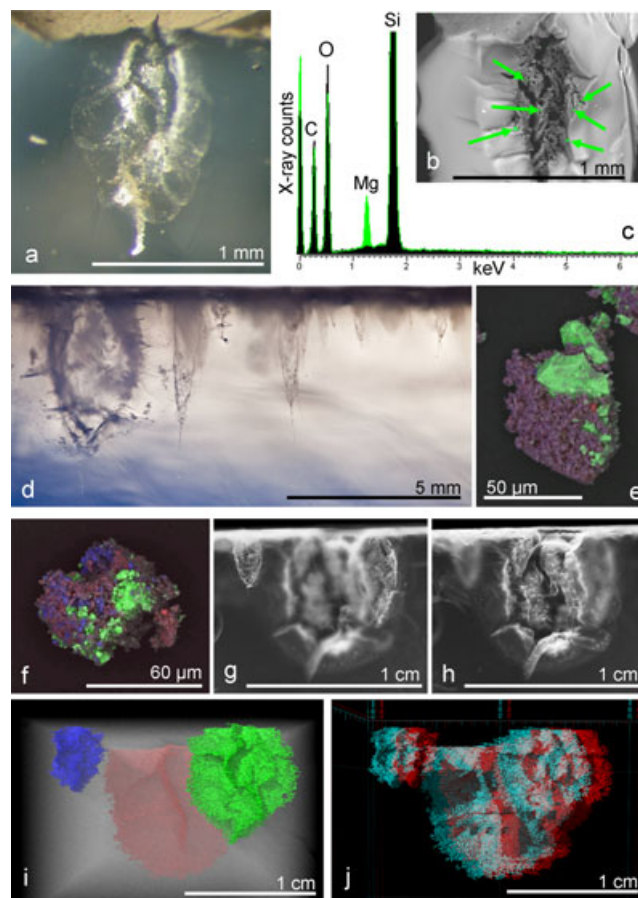


Fig. 10. Impacts by aggregates: a–c) lizardite, a porous natural monomineralic aggregate. Shot G310505#2: a) Type B track with short stylus. Note extensive radial fracturing, with inclusion of particle residues; b) backscattered electron image (BEI) of the same track as (a), with location of residue shown by a superimposed Mg EDX elemental map (green); c) EDX spectrum of lizardite residue in the left-hand petal-shaped fracture of (b), the residue spectrum is green, overlain on a spectrum of the surrounding aerogel (black); d–e) polydisperse diopside-pyrrhotite aggregates; d) impacts (shot G120709#1), showing a wide range of track sizes and variation from Type B with a broad proximal stylus, then one or more narrow distal styli, to large type C bulbous tracks with numerous lateral spikes, but no distal styli; e) combined color-coded X-ray maps (Mg blue, Ca red, Fe green) and BEI of a typical aggregate projectile; f–j) monodisperse olivine-diopside-pyrrhotite aggregates. f) X-ray maps (Mg blue, Ca red, Fe green) and BEI of a typical aggregate projectile; g, h) Shot G221208#2: optical micrographs of three Type C tracks (i, j) micro-CT reconstructions (i) is false-colored to differentiate three tracks and (j) is a red (left)–cyan (right) stereo anaglyph.

often with extensive intersecting petal-shaped fractures surrounding the open void of the bulb (see optical images in Figs. 10g and 10h, and micro-CT reconstructions in Figs. 10i and 10j). Fine-grained aggregates made of olivine, carbides, nitrides, alumina, and diamond generated large bulbous tracks (Figs. 11a

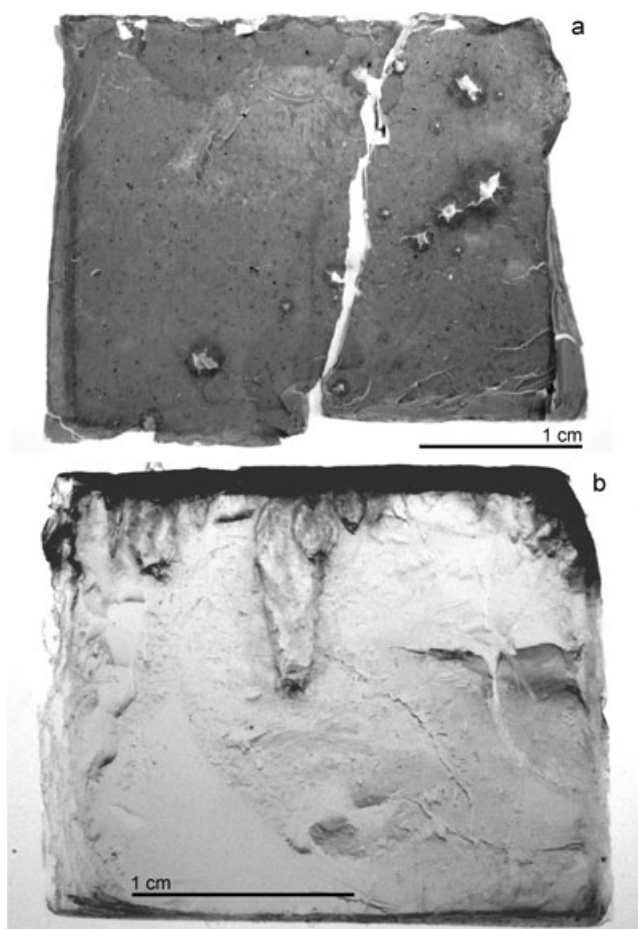


Fig. 11. Whole aerogel block showing multiple bulbous impacts by artificial presolar grain simulant aggregates (shot G300709#2). a) plan view showing entrance holes (b) lateral view of the right-hand portion of (a), showing bulbous tracks, overall shape changing with size, track length increases faster than width as track volume increases.

and 11b), with a shape gradation from small and very bulbous ($MW/TL > 0.66$, Type C) to large, narrow, and elongate ($MW/TL < 0.25$, Type B).

Organic Impacts

Table 2 and the plot of Fig. 4b clearly show that impacts by relatively small organic particles ($< 40 \mu\text{m}$?) are easily distinguished from those of crystalline monocrystalline anhydrous silicates, sulfides, and glasses, by their higher values of MW/TL . Glycine generated mainly short and squat bulbous Type C tracks (Figs. 12a–e), but also with some tapering to a very short stylus (Fig. 12d), as though really a squat, carrot-shaped Type A track, rather than truly bulbous Type B or C. We suggest these tracks be described as Type A*. Poly methylmethacrylate PMMA (Figs. 12f and 12g), Poly oxymethylene (Fig. 13) and Urea (Fig. 12h) also made broad bulbous tracks, and occasional broad tapering

tracks with a short tapering stylus (Fig. 12f, Type A*). We observed an increase in abundance of Type A* tracks in those made by larger PMMA projectiles: $80 \mu\text{m}$ particles created longer tracks with MW/TL approximately 0.28, as opposed to approximately 0.47 for approximately $30 \mu\text{m}$ impactors. Acrylate adhesive produced rounded bulbous Type C tracks with multiple small styli (Figs. 12i and 12j). Both sub-bituminous coal PSOC 1534 (Figs. 12k and 12l) and anthracite coal PSOC 1468 (Figs. 12m and 12n) also created bulbous Type C tracks, or showing a taper to a short stylus (e.g., Fig. 12n, Type A*). Fries et al. (2009) obtained organic G-band Raman signature from particles in the walls and styli of tracks produced by both these coals, implying that the broadly dispersed residue visible in optical micrographs is organic, and not hard, refractory nonorganic mineral matter, which makes up a small proportion of the coal.

Pure graphite made a very diverse range of broad track shapes (Fig. 4c), from very large tapering Type B (Fig. 12o), through bulbous Type B with multiple styli (Fig. 12q) to squat bulbous Type C (Fig. 12p). Fries et al. (2009) reported these samples as showing a high degree of structural amorphization as a result of hypervelocity impact into aerogel, implying pervasive processing on a very fine scale, as opposed to simple and nonintrusive coarse subgrain disaggregation.

DISCUSSION

The Creation of Type A Tracks

The creation of relatively simple elongate type A tracks by all of our glasses, crystalline anhydrous silicates, and crystalline sulfides (Fig. 4b) is no surprise, meeting expectations from previous experiments, numerical models, and Stardust observations (only 8% of Stardust Type A tracks have > 1 styli—see fig. 16 of Burchell et al. 2008a). Gentle curvature is seen in the distal part of the stylus in some glass and crystalline silicate tracks, which may result from irregular impactor shape or uneven surface ablation during capture, but the lack of track division into a bulb with numerous separate elongate styli (making broader and Type B tracks) in our experiments with low density aerogels (approximately 30 kg m^{-3}) may indicate perhaps that “intracrystal” strength is sufficient to prevent rapid fragmentation of these coarser crystalline grains. This may conversely imply that many Wild 2 particles are polycrystalline and substantially weaker (one-third of Stardust cometary dust tracks are broader, and of Type B). A larger number of divisions into multiple styli with numerous lateral spikes is, however, seen in experimental Type A tracks from

Table 2. Results from shots onto aerogel of approximately 30 kg m^{-3} density and Stardust-graded density aerogel (Flight Spare, FSSA or Flight Quality, FQSA), see Table 1 for sources for density data. The relative frequency of track types is derived from the larger tracks measured in each sample, and may differ for smaller tracks—e.g., the meteorite powders marked † also generated large numbers of very small Type A tracks, too small for precise measurement by our optical methods. Type A* tracks are short, squat, and have abnormally high MW/TL, see discussion below.

Projectiles	Projectile density (g cm^{-3})	Aerogel density (g cm^{-3})	Vel. km s^{-1}	Track width/length (avg \pm std. eva)	Track type relative abundance
Soda-lime glass beads	2.37 ^a	33	6.11	0.063 ± 0.023	A
		~ 30	6.40	0.059 ± 0.009	A
		FQSA	6.40	0.052 ± 0.014	A
Basalt glass NKT-1G	~ 2.8	FSSA	6.41	0.066 ± 0.018	A
Olivine (Fo ~ 88)	3.36 ^b	30	5.89	0.071 ± 0.009	A
Diopside	3.36 ^b	30	5.84	0.087 ± 0.020	A
Feldspar (An ~ 84)	2.72 ^b	~ 30	6.12	0.056	A
Pyrrhotite	4.63 ^b	31	6.39	0.080 ± 0.015	A
Cronstedtite	3.3 ^c	~ 30	6.12	0.028	A
Lizardite (porous)	$\sim 2.5^b$	30	5.96	0.342 ± 0.145	B > C > A
Meteorites					
Allende powder	2.79 bulk ^d	26	5.91	0.169 ± 0.098	B > A†
(fine pores in some)	3.30 grain ^d				
Murchison powder	2.25 bulk ^d	30	6.11	0.207 ± 0.142	B > C > A†
(polydisperse)	2.90 grain ^d				
Orgeuil powder	1.60 bulk ^d	30	6.21	0.257 ± 0.066	B
(fractured by sulfates?)	2.46 grain ^d				
Aggregates					
Diopside, coarse pyrrhotite; acrylic	~ 3 bulk ^e	~ 30	6.02	0.182 ± 0.142	A > B > C
Olivine, diopside and pyrrhotite, acrylic	~ 2.4 bulk ^e	FSSA	6.08	0.445 ± 0.115	C > B
Olivine, SiC, TiC, Si ₃ N ₄ , TiN, Al ₂ O ₃ and diamond	~ 2.4 bulk ^e	~ 30	6.09	0.469 ± 0.175	C > B
Organic materials					
Acrylic Pastel Fixative	$\sim 1.2^f$	27	6.42	0.593 ± 0.054	C
Poly methyl methacrylate	1.19 ^f	32	6.28	0.467 ± 0.057	C > A*
		~ 30	6.40	0.276 ± 0.046	B = A* > C
		FQSA	6.40	0.257 ± 0.141	B > C
Poly oxymethylene	1.43 ^a	~ 30	5.90	0.539 ± 0.101	C > > B > A*
Glycine	1.16 ^a	~ 30	6.06	0.419 ± 0.068	C > B > A*
¹⁵ N doped Urea	$\sim 1.4^a$	~ 30	6.04	0.941	C > A*
Coal (sub-bituminous)	$\sim 1.3^g$	31	6.22	0.427 ± 0.123	C > B > A*
Coal (anthracite)	1.6 ^h	FSSA	6.13	0.277	B
Graphite	$\sim 2.4^f$	32	6.33	0.389 ± 0.126	C = B

impacts onto higher density aerogel (60 kg m^{-3}) by enstatite (Figs. 6c–e) and feldspar (Figs. 7a and 7b). This contrasts with impacts by the glasses and olivines, which usually remain as elongate single styli even in impacts onto much denser aerogel (up to 110 kg m^{-3} , although complete particle fragmentation close to the target surface has been reported for 300 kg m^{-3} targets by Burchell et al. 2009a). This behavior of pyroxene and feldspar impacting on 60 kg m^{-3} aerogel may reflect partial fragmentation due to their well-developed internal crystallographic cleavage (e.g., Fig. 2e), a feature lacking in olivine and the glasses. The proximal track broadening seen in tracks formed by the pyroxene

and feldspar, and the dispersion of debris into spikes and fractures, imply that mechanical abrasion and breakage of the impactor, rather than expansion of released volatiles, is responsible for track expansion in such relatively refractory minerals. This may be in contrast to impact of pyrrhotite grains, where volatile migration into surrounding aerogel (and subsequent partial recombination with metallic droplets formed by impact) has been documented unambiguously by Ishii et al. (2008). It has been suggested that broadening of the proximal part of the stylus in sulfide impacts might be partly driven by volatile loss (Burchell et al. 2008a), leading to a shape transitional to Type B tracks (e.g.,

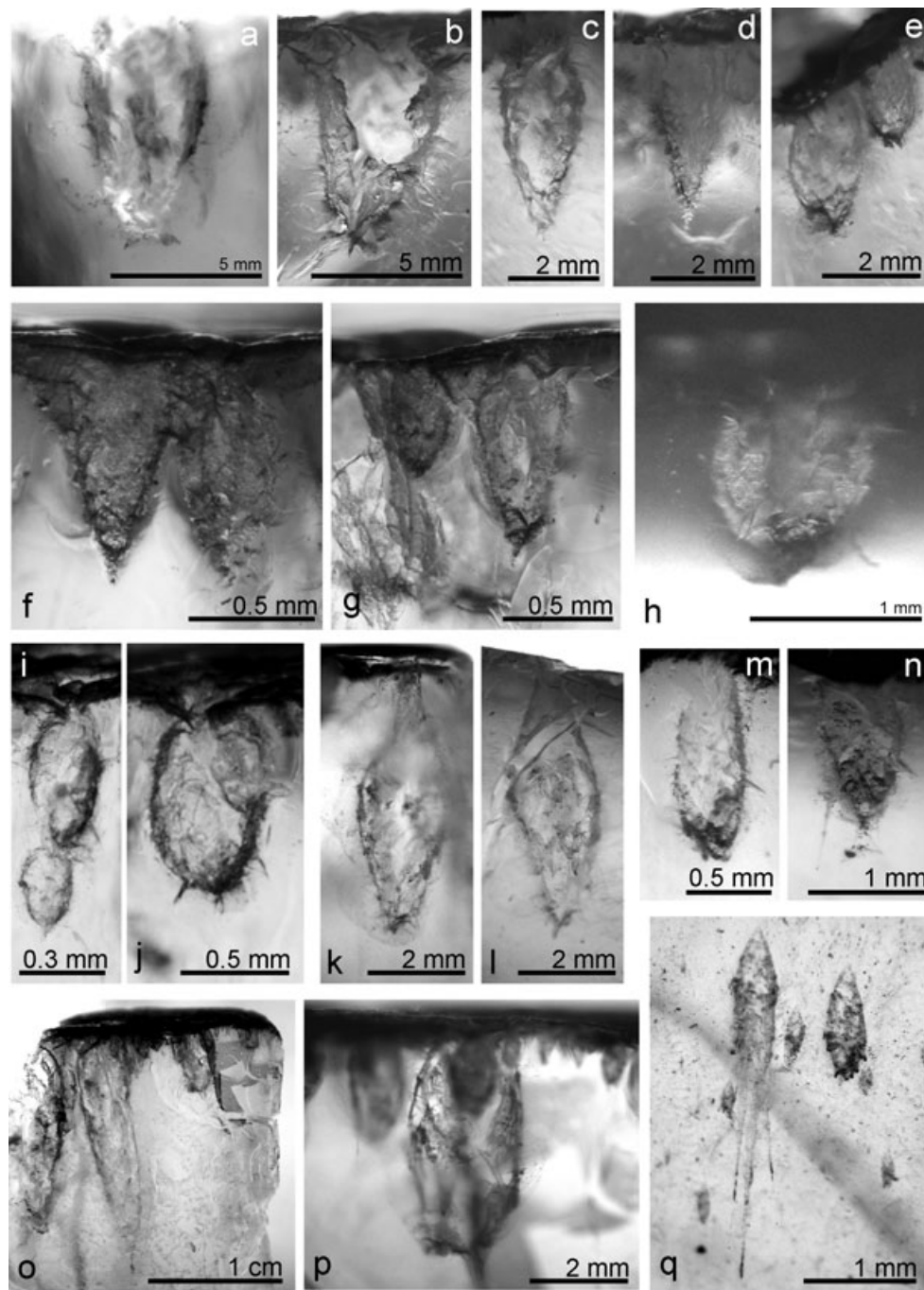


Fig. 12. Transmitted light optical micrographs of bulbous aerogel tracks created by impacts of organic materials. (a–e) Glycine (shot G011009#3). f, g) Poly methylmethacrylate (PMMA) (shot G281009#1). h) Urea (shot G191109#2). i, j) acrylate adhesive flakes (shot G210110#3). k, l) grains of anthracitic coal PSOC 1468 (shot G261108#1). m, n) grains of sub-bituminous coal PSOC 1534 (shot G040108#). (o, q); grains of pure graphite (shot G191207#2).

Fig. 7d). Nevertheless, our experiments show that most pyrrhotite tracks have similar overall MW/TL to those of anhydrous silicates (Fig. 4b), and have not been greatly widened.

However, the limitations of simple track morphological classification by MW/TL alone are

demonstrated by the tracks created by so many of our organic impactors. These small tracks have high MW/TL values, typical of the shapes usually described as bulbous Type B to C tracks. They do not, however, have a rounded bulbous distal region, but instead show a tapering outline from broadest width close to the aerogel

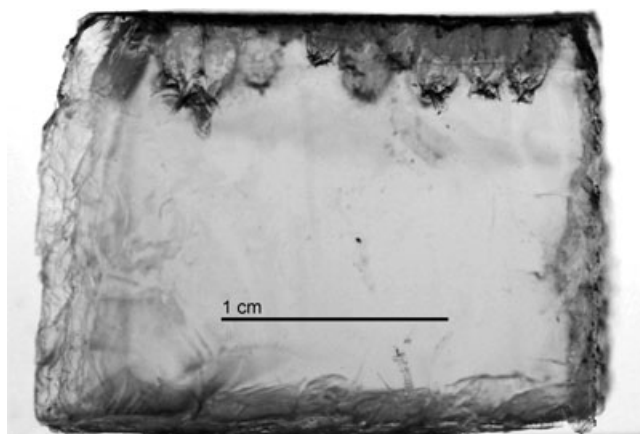


Fig. 13. Transmitted light optical micrograph of bulbous Type C aerogel tracks created by impacts of grains of poly oxymethylene (shot G191109#3).

surface down to a very short stylus. Their outline is that of a short and squat Type A, and we therefore suggest that they should be described as Type A*.

The Roles of Vapor Expansion and Mechanical Disaggregation

Published transmission electron microscope (TEM) images of captured hydrous silicate particles (approximately 15% H₂O by weight in lizardite and approximately 9% in cronstedtite) have shown that much of the particle mass is lost during creation of their tracks, with amorphization, melting, and vesiculation within the surface of the remaining particle (Okudaira et al. 2004, 2005), although the center still may retain original structure (Noguchi et al. 2007). This implies that both lizardite and cronstedtite must lose abundant water as vapor, yet the tracks created by these impacts of cronstedtite and lizardite were not described as bulbous in shape, even though Yano et al. (1999) have shown that lower velocity ice impacts do yield shallow bulbous tracks. Our own track from a cronstedtite impact (Fig. 7g) is again of Type A, long and narrow, showing no evidence of broadening of the stylus due to volatile expansion. However, tracks from our lizardite grains are of all types (Fig. 8), but mainly of Type B (plotted in Fig. 4e). Why is there a wider range of track shapes than previously seen, when the projectile has essentially the same chemical composition and volatile content? We suggest that the more complex internal structure of our new lizardite particles may be responsible for the complex track formation mechanism. Our lizardite has a porous internal aggregate structure (Fig. 3a), yet is neither particularly low in density, nor very weak. The particles are sufficiently strong to survive acceleration in

the LGG, meeting the target as a wide range of grain sizes including as coarse aggregates, and giving the very broad range of foil crater sizes seen in our earlier experiments (Kearsley et al. 2009). In light of the earlier studies, we therefore suggest that the bulbous tracks in Fig. 8 were not created by impact-driven release and expulsion of structurally bound water (as was suggested for one of our lizardite impacts, by Hörz et al. 2006), but reflect a large degree of mechanical deformation and disintegration of aggregate particles, resulting in broadening of the impacting particle and dispersion of fragments, as seen in Fig. 10c. The precise mechanism for disruption of an aggregate material entering aerogel under Stardust encounter conditions may need further numerical modeling. Do impactor surface irregularity and pore space encourage aggressive intrusion of compressed aerogel, or simply act as mechanical stress concentrators during impact? Either might cause breakup and subsequent, relatively unconfined, lateral expansion of even a relatively strong and hard aggregate. Whether rapid emplacement of fragments (e.g., from hydrous silicate aggregates) around a bulbous track results in more or less damage to the individual subgrains is not yet known, but should be investigated.

Impacts of powdered carbonaceous chondrite meteorite samples (natural aggregates) also yielded a range from Type A, through numerous broad Type B of a wide range of sizes, to a few transitional to Type C tracks. Even though Allende lacks very fine hydrous minerals (abundant in Murchison and Orgueil) particles from all three meteorites yield broad tracks. This again suggests that expulsion of released volatile material is not the sole cause of track expansion, and the fine porous aggregate nature of Allende matrix may act in a similar way to the lizardite aggregates described above. There is thus no simple clear correlation between the mineralogy, grain size, porosity, and density of the bulk meteorite projectile material and the track shape. Instead, the diversity of track shapes is probably due to markedly different individual projectile properties, which itself reflects the highly heterogeneous nature of these carbonaceous chondrites at a scale of a few micrometers.

Bulbous Tracks, Aggregates, Organic Matter, and the Role of Volatile Release

Our experiments with artificial analog aggregate particles (Fig. 3g) containing coarser mineral subgrains in a finer mineral matrix, bound together by organic matter (Fig. 10e), now confirm the suggestions of Trigo-Rodríguez et al. (2008) and Kearsley et al. (2009) that the bulb and multiple styli of Type B tracks (Fig. 10d) can be made by deformation, fragmentation, and dispersal of polydisperse silicate and sulfide aggregates

during impact on aerogel. We also suspected that Type C tracks might be produced by impact of artificial aggregates of monodisperse fine mineral powders (Fig. 3h), and this too is now confirmed (Figs. 10f–j and 11). Here, we must introduce a caveat: results from organic-bound artificial aggregates cannot conclusively prove that bulb formation is entirely due to mechanical deformation and separation of mineral subgrains. These particular experiments do not preclude a role for expansion of volatiles released from the acrylate adhesive. The production of bulbous tracks by cocoa powder (Hörz et al. 2006) also raised a similar question. What is responsible: particle structure, composition, or both? Other shots demonstrate that acrylate alone can itself create bulbous Type C tracks (Figs. 12i and 12j), as do other pure organic materials (Figs. 4c, 12, and 13) such as POM, PMMA, glycine, urea, nylon sabot fragments from the LGG, and coals.

Trigo-Rodríguez et al. (2008) and Iida et al. (2010) have suggested that expansion of volatile material released from unstable materials should be relatively unimportant in the creation of bulbous tracks. The behavior of very soft graphite (Figs. 4c and 12), which contains no volatile components, yet produces Type B and C tracks, confirms this—clearly showing that low particle strength is sufficient to create a bulbous shape.

Is the same mechanical failure responsible for the bulbous tracks made by organic materials? It is possible that some, especially if softened due to their low melting point, may simply spread during impact, and hence behave like weaker aggregate particles. Although acrylates are relatively strong polymers, widely used as glazing material, they have a low resistance to surface abrasion and decompose at a relatively low temperature (approximately < 500 K). Some of their original composition survives impact into aerogel, as revealed by Raman spectroscopy of fragments within styli (Burchell et al. 2004), but we do not yet know whether the impactor size reduction is entirely due to mechanical abrasion, or partly due to thermal decomposition, which will be accompanied by volatile evolution.

Our experiments therefore demonstrate conclusively that weak and/or aggregate structure can promote bulb formation, but we still cannot yet rule out any contribution of volatile release from organic materials.

Is Track Morphology Simply Controlled by Impacting Particle Density?

The multiple possible combinations of impactor composition, density, target density, and impact velocity control track morphology in a complex manner. For example, it is easy to demonstrate the effect of changing target density on the length and volume of Type A tracks

in the relatively high density aerogels ($60\text{--}180\text{ kg m}^{-3}$) described by Burchell et al. (2001, 2009a). This has now also been seen in lower density aerogels impacted at approximately 5 km s^{-1} , where the same soda-lime glass beads penetrate almost twice as far into 13 kg m^{-3} aerogel as in a 30 kg m^{-3} target (Burchell et al. 2009a). Where robust impacting particles have similar physical properties, such as hardness, melting, and dissociation temperatures, for impacts at the same velocity, there does also seem to be a relationship between particle kinetic energy (dependent on size and density, hence mass), and the length of track and volume of aerogel displaced (Burchell et al. 2009a). However, does contrast between density of the impacting particle and a constant aerogel target exert the dominant control on track shape? Iida et al. (2010) and Niimi et al. (2011) have suggested that the larger scale features of aerogel track shape may directly reflect the impacting particle density, and that low-density particles are responsible for Type B and C tracks. Studies of impacts on Stardust-type aluminum foil by materials with a wide range of density, approximately 1 to approximately 8 g cm^{-3} (Kearsley et al. 2008, 2009), have shown that crater shape, particularly the ratio between depth and diameter, certainly is strongly influenced by impactor density, although both particle shape and internal structure can also be important. However, impact processes on a relatively dense (approximately 2.8 g cm^{-3}) and ductile substrate such as aluminum foil are very different to those in low density aerogel. Although low density aggregate particles may create irregular shapes on foil (e.g., fig. 25 of Kearsley et al. 2008; fig. 6 of Kearsley et al. 2009), there is little opportunity for tightly packed constituent subgrains to separate and disperse widely to create further structural complexity, as occurs in aerogel. For impacts onto aerogel, there is good evidence that robust particles of higher density can make longer Type A aerogel tracks than lower density particles of the same size (Niimi et al. 2011), although the depth of penetration may also partly depend upon the degree of ablation and abrasion suffered (for example, compare the alumina impacts of Hörz et al. [2009] with the glycine of Nixon et al. [2012]), and depth may therefore not be related to the particle density alone. Crucially, our experimental creation of Type B and C tracks from relatively high density (approximately 2.4 g cm^{-3}) natural and artificial aggregates and graphite, all impacted onto aerogel of low density (approximately 30 kg m^{-3}) has now clearly demonstrated that bulk impactor density is not the only controlling factor over the track geometry. The overall density of our artificial aggregates is similar to that of soda-lime glass (known from many, many experiments to create Type A tracks). Hence, track shape alone cannot be a reliable indicator of the impactor density or porosity, as was implied by Iida

et al. (2010) and Niimi et al. (2011). Instead, we have shown that impactor structure exerts a more significant control over track shape development. Interestingly, our experiments may also suggest that overall size of an impacting aggregate or organic particle can influence the resulting track shape, with some larger particles apparently creating elongate bulbous tracks with greater length to maximum width ratio (lower MW/TL) than smaller tracks in the same target (e.g., aggregates in Fig. 11b, coal in Figs. 12o and 12p). This may reflect pervasive flattening and/or break-up for the entire volume of a small weak, or soft, impactor during the initial portion of capture and track formation (i.e., near the aerogel surface). A larger particle of similar properties may experience only partial exfoliation and surface mechanical abrasion in the shallower part of the aerogel before it is slowed, thereby preventing complete disruption, and allowing the fragmenting core to penetrate to a relatively deep level, making a rather longer track.

Particle Mass Loss During Capture, and Recognition of Organic Impactors

As suspected in earlier studies (e.g., Hörz et al. 2000), the interaction between particle composition and impact velocity may also play an important role in controlling grain preservation and aerogel track shape. This has become particularly apparent in the diverse responses of impactors with very different melting and dissociation temperatures. Burchell et al. (2001) and Fig. 9 demonstrated that although there is progressive loss of soda-lime particle volume as impact velocity is increased from 1 to $>6 \text{ km s}^{-1}$, the track retains a long and narrow Type A morphology. Burchell et al. (2009b) showed that polystyrene beads leave well-defined Type A tracks when impacted on low density aerogel at 1.2 km s^{-1} . However, subsequent reexamination of tracks from similar polystyrene beads impacted at approximately 6 km s^{-1} (Nixon et al. 2012) shows that these particles undergo substantial mass loss, and has revealed a rather different, much broader, track shape, like that which we have here designated as Type A*. These high speed tracks therefore do not have a simple broad bulbous cavity like so many illustrated herein. Instead, small particles of polystyrene, glycine, PMMA (and polyethyl methacrylate PEMA, Burchell et al. 2004), may create squat carrot shapes with a maximum width developing shortly after entry into the aerogel, giving MW/TL much greater than the previously defined range for Type A tracks. Our most recent results also suggest that organic impactor size plays a role in controlling these track shapes, larger organic particles creating narrower and longer Type A* tracks than smaller particles of the same composition. We do not

know whether there is increase in both track width and length, or merely width, as impact velocity increases, and further work is clearly needed to quantify the shape characteristics of impacts by different types and sizes of organic materials. In the analysis of the Stardust cometary dust tracks, Burchell et al. (2008a) also reported that Type A tracks with the shortest track lengths had wider track widths than normal for Type A (see figs. 17 and 18 in Burchell et al. 2008a). Are these Type A*? No detailed high-resolution imaging of these shortest Stardust cometary dust tracks has been published, and perhaps a population of Wild 2 dust impacts by small organic particles remains to be investigated?

Evaluating the Size and Mass of Particles Making Type B and C Tracks

Burchell et al. (2001) established that impacts by a relatively robust material such as soda-lime glass show a near linear relationship between the impacting particle volume (hence projectile mass and kinetic energy) and the volume of a Type A aerogel track (i.e., excavated mass). It was therefore possible to use this type of volumetric measurement to determine the size of many particles collected by Stardust (Burchell et al. 2008a). However, Hörz et al. (2006) noted that the interpretation of particle size responsible for bulbous tracks, which make up about half of the larger Stardust impacts, was not well-constrained, as appropriate calibration experiments had not been possible. Unfortunately, the variable degree of break-up seen during violent LGG acceleration of artificial aggregate projectiles still prevents such material being used as reliable size calibration standards for bulbous Type B and C tracks. We could, however, use other projectiles that are more robust, and which can arrive at the aerogel target as a monodisperse cloud. For example, monodisperse PMMA spheres yield aluminum foil craters of a narrow size range (i.e., they are proven to survive LGG acceleration intact) and are known to create bulbous tracks in aerogel (e.g., Fig. 3c).

The differing size and depth profile of craters produced by soda-lime glass and PMMA shot onto aluminum foil (Kearsley et al. 2007) suggests that these two projectile materials do not have equivalent excavation efficiencies per unit of kinetic energy when impacted on this substrate. PMMA yields narrower and shallower craters. We do not yet know whether tracks in aerogel also show a clear difference in volume between the two impactor materials, although their tracks are clearly of different shape. Using LSCM or synchrotron X-ray microtomography, it should be possible to make a precise measurement of track volumes created by grains of known mass (and kinetic energy), and compare sizes

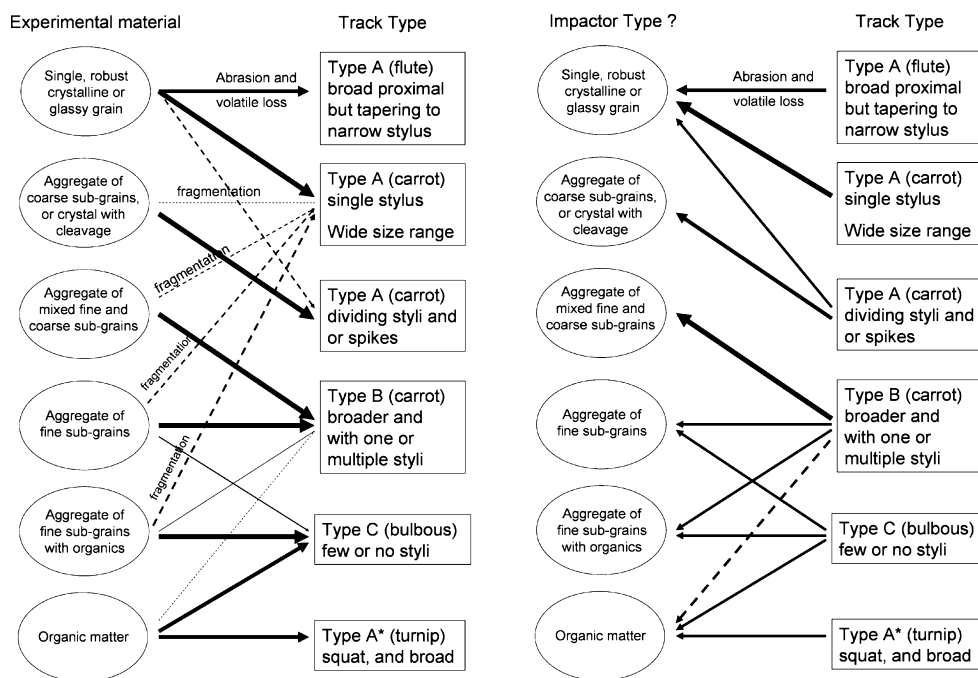


Fig. 14. a) Track morphology created by differing types of experimental projectiles, bolder lines indicate more frequent occurrence of the track type from this origin. Note that many aggregate projectiles fragmented during flight, resulting in creation of many smaller and simpler tracks. b) A suggested interpretation of Stardust track morphology in terms of the type of impactor responsible, based on our experimental evidence.

for soda-lime glass (Type A) tracks and PMMA (Type C) tracks. We suggest that these experiments would then provide a better impactor size and mass calibration for the bulbous Stardust tracks.

How to Interpret Particle Properties from Track Type

In Fig. 14 we summarize our conclusions about the link between impactor properties and aerogel track shape (Fig. 14a), and invert this argument to give a scheme for the recognition of impactor properties from characteristic track shapes (Fig. 14b). Projectile fragmentation during acceleration in the LGG is responsible for the diverse track shapes that can be produced by shot of a single aggregate type in Fig. 14a. Conversely, it is important to note that a single track type could be interpreted as the result of impact by any one of several types of impactor (Fig. 14b).

CONCLUSIONS: IMPLICATIONS FOR INTERPRETATION OF WILD 2 DUST

Our LGG experiments have now successfully reproduced the range of aerogel track morphology seen in the Stardust collector (Fig. 15), using projectiles that are probably appropriate analogs of the materials extracted from tracks actually made by Wild 2 comet

dust. The close correspondence in track shape between our experimental impacts onto aerogel of uniform 30 kg m^{-3} and those onto Stardust type aerogel (of graded $5\text{--}50 \text{ kg m}^{-3}$ density) using the two very different materials plotted in Fig. 4f suggests that our results should also be directly comparable to the shapes of Wild 2 dust tracks in the Stardust collector aerogel, although there may be a minor difference in absolute track size.

Type A tracks can be produced by a wide range of mechanically robust silicate and sulfide impactors, although the release of volatile sulfur can broaden the proximal part of the track, creating a throat and main cavity above a tapering stylus. Well-developed crystallographically controlled cleavage planes may aid fragmentation and emplacement of debris into lateral/radial spikes and fractures, for example, by pyroxene and feldspar impactors.

Experimental high speed impacts by low density, organic particles produce broad tapering Type A* tracks, wider than the typical Type A, but without a true bulbous proximal cavity. They resemble a subpopulation of Type A tracks with short track lengths, known from Stardust—but which do not appear to have been considered beyond a note in Burchell et al. (2008a), and which are a suitable subject for further studies to more clearly define their shape and origin.

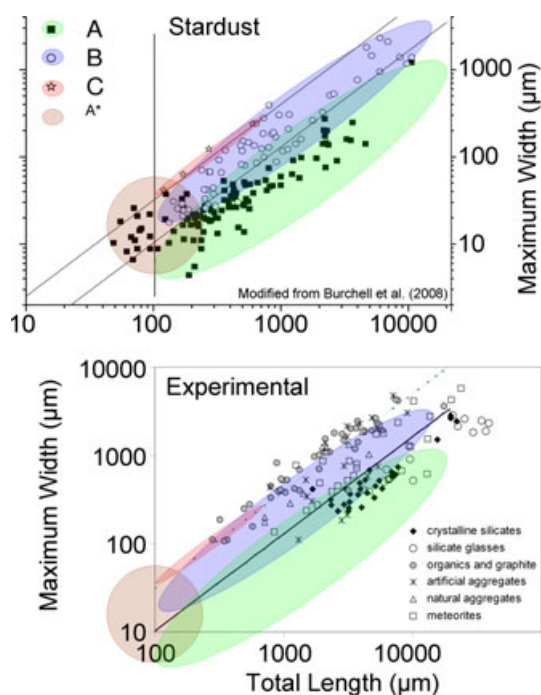


Fig. 15. Comparison of experimental aerogel tracks with those created by impact of Wild 2 cometary dust on the Stardust collector. Total Length axes are aligned across the two parts of the plot, revealing that many of the experimental tracks are larger than those of Stardust, yet retain the same overall shapes. The color-coded fields for Types A, B, C, and A* are drawn from the plot for the Stardust collector, and are also superimposed in the same position on the experimental data. Note that the experimental impacts by meteorite powders are a close match to Stardust Type B tracks.

We have shown that internal grain-size range within impacting particles exerts a strong control on aerogel track shape. Our experimental evidence shows that diverse (polydisperse) subgrain size within an aggregate material (natural or artificial) encourages Type B track formation, with multiple small styli penetrating onward from the distal region of a bulbous segment. Comparison to impacts by relatively strong and dense aggregates indicates that large Stardust Type B tracks were not necessarily made by weak and low density particles, as suggested by other authors. It should therefore not be assumed that Type B and C Stardust tracks were all made by “fluffy,” very high porosity particles.

Fine-grained aggregates, with subgrain size all of micrometer scale, generate broad bulbous Type B and C tracks, surrounded by extensive intersecting aerogel fractures containing impactor debris. The creation of the broadest Type C tracks by a wide range of organic species may indicate that volatile expansion plays some role in the creation of Type B and C aerogel tracks, especially as some of these polymers are relatively strong, and might not be expected to undergo greater mechanical break-up

than silicate-rich aggregates. Although volatile-free graphite impacts show the importance of mechanical disaggregation in the creation of some bulbous tracks, we still await successful shots of sintered (rather than glued) artificial anhydrous aggregate particles.

Future Work

Our new experimental tracks now also offer an opportunity to study the detailed distribution and preservation of known impactor materials in bulbous tracks, for example, to compare them with materials analyzed in the Type B Stardust track by Leroux et al. (2008). Previous experiments have given evidence of impactor abrasion for glasses (Burchell et al. 2001), sulfides (Ishii et al. 2008), and even refractory oxides (Hörz et al. 2009), and the dispersion of soft organic projectiles (Hörz et al. 1998). Our future work will consider the spatial distribution of dispersed aggregate components in the walls and external fracture systems of Type B and C tracks; the state of fine subgrain preservation including evidence for elemental fractionation and dispersion (also with new projectiles of pentlandite and calcite); the alteration of known organic species by the impact process including migration of primary organics and their pyrolytic products; the fractionation, migration, and mixing of labeled light element stable isotopic signatures from both silicate and organic species.

Acknowledgments—We thank NASA, Peter Tsou and Steve Jones of JPL, and Kyoko Okudaira for aerogel to use in experiments; STFC for funding the hypervelocity impact facilities and their staff at The University of Kent; NHM for access to electron microscopy and microanalysis facilities, for excellent work by the photographic unit, and Richie Abel in the Electron Microscopy and Mineral Analysis division for the micro-CT scanning and image rendering. Fred Hörz and Brad de Gregorio made such insightful and helpful reviews that we must thank them for driving us to greatly improve this publication. Parts of this work were performed under the auspices of the U.S. DOE by LLNL under Contract DE-AC52-07NA27344. This work was supported by grants: NASA NNH07AG46I to HAI & LDRD 09-ERI-004 to JPB.

Editorial Handling—Dr. Michael Zolensky

REFERENCES

- A'Hearn M. F., Belton M. J. S., Delamere W. A., Feaga L. M., Hampton D., Kissel J., Klaasen K. P., McFadden L. A., Meech K. J., Melosh H. J., Schulz P. J., Sunshine J. M., Thomas P. C., Veverka J., Wellnitz D. D., Yeomans D. K.,

- Besse S., Bodewits D., Bowling T. J., Carcich B. T., Collins S. M., Farnham T. L., Groussin O., Hermalyn B., Kelley M. S., Li J. Y., Lindler D. J., Lisse C. J., McLaughlin S. A., Merlin F., Protopapa S., Richardson J. E., and Williams J. E. 2011. EPOXI at comet hartley 2. *Science* 332:1396–1400.
- Atria J. V., Zeng S., Rusinko F., and Schobert H. H. 1994. Novel approach to the production of graphite from anthracite. *American Chemical Society Division of Fuel Chemistry Preprints* 39:884–888.
- Barrett R. A., Zolensky M. E., Hörz F., Lindstrom D. J., and Gibson E. K. 1992. Suitability of silica aerogel as a capture medium for interplanetary dust (abstract). Proceedings, 22nd Lunar and Planetary Science Conference. pp. 203–212.
- Beer E. H., Podolak D., and Prialnik D. 2006. The contribution of icy grains to the activity of comets I. Grain lifetime and distribution. *Icarus* 180:473–485.
- Brearely A. J. and Jones R. H. 1998. Chondritic meteorites. In *Planetary materials*, edited by Papike J. J. Reviews in Mineralogy, vol. 36. Washington, D.C.: Mineralogical Society of America. pp. 3-01–3-398.
- Brownlee D., Tsou P., Aléon J., Alexander C. M. O'D., Araki T., Bajt S., Baratta G. A., Bastien R., Bland P., Bleuët P., Borg J., Bradley J. P., Brearely A., Brenker F., Brennan S., Bridges J. C., Browning N., Brucato J. R., Brucato H., Bullock E., Burchell M. J., Busemann H., Butterworth A., Chaussidon M., Chevront A., Chi M., Cintala M. J., Clark B. C., Clemett S. J., Cody G., Colangeli L., Cooper G., Cordier P. G., Daghljan C., Dai Z., D'Hendecourt L., Djouadi Z., Dominguez G., Duxbury T., Dworkin J. P., Ebel D., Economou T. E., Fairey S. A. J., Fallon S., Ferrini G., Ferroir T., Fleckenstein H., Floss C., Flynn G., Franchi I. A., Fries M., Gainsforth Z., Gallien J.-P., Genge M., Gilles M. K., Gillet P., Gilmour J., Glavin D. P., Gounelle M., Grady M. M., Graham G. A., Grant P. G., Green S. F., Grossemey F., Grossman L., Grossman J., Guan Y., Hagiya K., Harvey R., Heck P., Herzog G. F., Hoppe P., Hörz F., Huth J., Hutcheon I. D., Ishii H., Ito M., Jacob D., Jacobsen C., Jacobsen S., Joswiak D., Kearsley A. T., Keller L., Khodja H., Kilcoyne A. L. D., Kissel J., Krot A., Langenhorst F., Lanzirotti A., Le L., Leshin L., Leitner J., Lemelle L., Leroux H., Liu M.-C., Luening K., Lyon I., MacPherson G., Marcus M. A., Marhas K., Matrajt G., Meibom A., Mennella V., Messenger K., Mikouchi T., Mostefaoui S., Nakamura T., Nakano T., Newville M., Nittler L. R., Ohnishi I., Ohsumi K., Okudaira K., Papanastassiou D. A., Palma R., Palumbo M. O., Pepin R. E., Perkins D., Perronnet M., Pianetta P., Rao W., Rietmeijer F., Robert F., Rost D., Rotundi A., Ryan R., Sandford S. A., Schwandt C. S., See T. H., Schlutter D., Sheffield-Parker J. A., Simionovici S., Sitnitsky S. I., Snead C. J., Spencer M. K., Stadermann F. J., Steele A., Stephan T., Stroud R., Susini J., Sutton S. R., Taheri M., Taylor S., Teslich N., Tomeoka K., Tomioka N., Toppini A., Trigo-Rodríguez J. M., Troadec D., Tsuchiyama A., Tuzzolino A. J., Tyliczek T., Uesugi K., Velbel M., Vellenga J., Vicenzi E., Vincze L., Warren J., Weber I., Weisberg M., Westphal A. J., Wirick S., Wooden D., Wopenka B., Wozniakiewicz P. A., Wright I., Yabuta H., Yano H., Young E. D., Zare R. N., Zega T., Ziegler K., Zimmerman L., Zinner E., and Zolensky M. 2006. Comet Wild 2 under a microscope. *Science* 314:1711–1716.
- Burchell M. J. and Kearsley A. T. 2009. Short-period Jupiter family comets after Stardust. *Planetary and Space Science* 57:1146–1161.
- Burchell M. J. and Thomson R. 1996. Intact hypervelocity particle capture in aerogel in the laboratory. In *Shock Compression of Condensed Matter-1997, Conference Proceedings* 429. New York: AIP Press. pp. 1155–1158.
- Burchell M. J., Cole M. J., McDonnell J. A. M., and Zarnecki J. C. 1999a. Hypervelocity impact studies using the 2 MV Van de Graaff dust accelerator and two stage light gas gun of the University of Kent at Canterbury. *Measurement Science & Technology* 10:41–50.
- Burchell M. J., Thomson R., and Yano H. 1999b. Capture of hypervelocity particles in aerogel: In ground laboratory and low earth orbit. *Planetary and Space Science* 47:189–204.
- Burchell M. J., Creighton J. A., Cole M. J., Mann J., and Kearsley A. T. 2001. Capture of particles in hypervelocity impacts in aerogel. *Meteoritics & Planetary Science* 36:209–221.
- Burchell M. J., Creighton J. A., and Kearsley A. T. 2004. Identification of organic particles via Raman techniques after capture in hypervelocity impacts on aerogel. *Journal of Raman Spectroscopy* 35:249–253.
- Burchell M. J., Graham G. A., and Kearsley A. 2006a. Cosmic dust collection in aerogel. *Annual Review of Earth and Planetary Sciences* 34:385–418.
- Burchell M. J., Mann J., Creighton J. A., Kearsley A. T., and Franchi I. A. 2006b. Identification of minerals and meteoritic materials via Raman techniques after capture in hypervelocity impacts on aerogel. *Meteoritics & Planetary Science* 41:217–232.
- Burchell M. J., Fairey S. A. J., Wozniakiewicz P., Brownlee D. E., Hörz F., Kearsley A. T., See T. H., Westphal A., Green S. F., and Trigo-Rodríguez J. M. 2008a. Characteristics of cometary dust tracks in Stardust aerogel and laboratory calibrations. *Meteoritics & Planetary Science* 43:23–40.
- Burchell M. J., Pushkin N., Kearsley A. T., and Hörz F. 2008b. Tracks in Stardust cometary aerogels: What they tell us about cometary particle structure and size distribution (abstract #8126). 2008 Asteroids, Meteors and Comets Conference. CD-ROM.
- Burchell M. J., Fairey S. A. J., Foster N. J., and Cole M. J. 2009a. Hypervelocity capture of particles in aerogel: Dependence on aerogel properties. *Planetary and Space Science* 57:58–70.
- Burchell M. J., Foster N. J., Ormond-Prout J., Dupin D., and Armes S. P. 2009b. Extent of thermal ablation suffered by model organic microparticles during aerogel capture at hypervelocities. *Meteoritics & Planetary Science* 44:1407–1419.
- Burchell M. J., Cole M. J., Price M. C., and Kearsley A. T. 2011. Ice Impacts on aerogel and Stardust Al foil (abstract). *Meteoritics & Planetary Science* 46(S1):A34.
- Consolmagno G. J., Britt D., and Macke R. J. 2008. The significance of meteorite density and porosity. *Chemie der Erde (Geochemistry)* 68:1–29.
- Corrigan C., Zolensky M. E., Dahl J., Long M., Weir J., Sapp C., and Burkett P. J. 1997. The porosity and permeability of chondritic meteorites and interplanetary dust particles. *Meteoritics & Planetary Science* 32:509–515.
- Cottin H., Bénilan Y., Gazeau M.-C., and Raulin F. 2004. Origin of cometary extended sources from degradation of

- refractory organics on grains: Polyoxymethylene as formaldehyde parent molecule. *Icarus* 167:397–416.
- Deer W. A., Howie R. A., and Zussman J. 1992. *An introduction to the rock-forming minerals*, 2nd edition. Harlow: Pearson Education Limited, 712 p.
- Domínguez G., Westphal A. J., Jones S. M., and Phillips M. J. F. 2004. Energy loss and impact cratering in aerogels: Theory and experiment. *Icarus* 172:613–624.
- Ebel D. S., Greenberg M., Rivers M. L., and Newville M. 2009. Three-dimensional textural and compositional analysis of particle tracks and fragmentation history in aerogel. *Meteoritics & Planetary Science* 44:1445–1463.
- Foster N. J. 2006. *Synthesis of silica aerogel and its application as a hypervelocity dust capture cell*. MSc thesis, University of Kent, Canterbury, UK.
- Foster N. J., Burchell M. J., Creighton A. J., and Kearsley A. T., Stardust Organics PET. 2007. Does capture in aerogel change carbonaceous Raman D and G bands? (abstract #1647). 38th Lunar and Planetary Science Conference. CD-ROM.
- Foster N. J., Kearsley A. T., Burchell M. J., Wozniakiewicz P. J., Creighton J. A., and Cole M. J. 2008. Analysis of hydrous phyllosilicates in Stardust type B tracks (abstract #8209). 2008 Asteroids, Meteors and Comets Conference. CD-ROM.
- Fries M., Burchell M., Kearsley A., and Steele A. 2009. Capture effects in carbonaceous material: A Stardust analogue study. *Meteoritics & Planetary Science* 44:1465–1474.
- Gounelle M. and Zolensky M. E. 2001. A terrestrial origin for sulfate veins in CI1 chondrites. *Meteoritics & Planetary Science* 36:1321–1329.
- Graham G. A., Chater R. J., Kearsley A. T., Burchell M. J., and Bradley J. P. 2003. Extraction of particles impacted into silica aerogel. *Geophysical Research Abstracts* 5:04087.
- Graham G. A., Kearsley A. T., Butterworth A. L., Bland P. A., Burchell M. J., McPhail D. S., Chater R. J., Grady M. M., and Wright I. P. 2004a. Extraction and microanalysis of cosmic dust collected during sample return missions: Laboratory simulations. *Advances in Space Research* 34:2292–2298.
- Graham G. A., Grant P. G., Chater R. J., Westphal A. J., Kearsley A. T., Snead C., Domínguez G., Butterworth A. L., McPhail D. S., Bench G., and Bradley J. P. 2004b. Investigation of ion beam techniques for the analysis and exposure of particles encapsulated by silica aerogel: Applicability for Stardust. *Meteoritics & Planetary Science* 39:1461–1473.
- Graham G. A., Sheffield-Parker J., Bradley J. P., Kearsley A. T., Dai Z. R., Mayo S. C., Teslich N., Snead C., Westphal A. J., and Ishii H. 2005. Electron beam analysis of micrometeoroids captured in aerogel as Stardust analogues (abstract #2078). 36th Lunar and Planetary Science Conference. CD-ROM.
- Greenberg M. and Ebel D. S. 2010. Laser scanning confocal microscopy of comet material in aerogel. *Geosphere* 6:515–523.
- Hörz F. 2012. Cratering and penetration experiments in aluminum and teflon: Implications for space exposed surfaces. *Meteoritics and Planetary Science* 47.
- Hörz F., Cintala M. J., Zolensky M. E., Bernhard R. B., Davidson W. E., Haynes G., See T. H., Tsou P., and Brownlee D. E. 1998. Capture of hypervelocity particles with low density aerogel. NASA TM-98–201792. 58 p.
- Hörz F., Zolensky M. E., Bernhard R. P., See T. H., and Warren J. L. 2000. Impact features and projectile residues in aerogel exposed on Mir. *Icarus* 147:559–579.
- Hörz F., Bastien R., Borg J., Bradley J. P., Bridges J. C., Brownlee D. E., Burchell M. J., Cintala M. J., Dai Z. R., Djouadi Z., Domínguez G., Economou T. E., Fairey S. A. J., Floss C., Franchi I. A., Graham G. A., Green S. F., Heck H., Hoppe P., Huth J., Ishii H., Kearsley A. T., Kissel J., Leitner J., Leroux H., Marhas M., Messenger K., Schwandt C. S., See T. H., Snead S., Stadermann F. J., Stephan T., Stroud R., Teslich N., Trigo-Rodríguez J. M., Tuzzolino A. J., Troadec D., Tsou P., Warren J., Westphal A., Wozniakiewicz P. J., Wright I., and Zinner E. 2006. Impact features on Stardust: Implications for comet 81P/Wild 2 dust. *Science* 314:1716–1719.
- Hörz F., Cintala M. J., See T. H., and Nakamura-Messenger K. 2009. Penetration tracks in aerogel produced by Al₂O₃ spheres. *Meteoritics & Planetary Science* 44:1243–1264.
- Iida Y., Tsuchiyama A., Kadono T., Sakamoto K., Nakamura T., Uesugi K., Nakano T., and Zolensky M. 2010. Three-dimensional shapes and Fe contents of Stardust impact tracks: A track formation model and estimation of comet Wild 2 coma dust particle densities. *Meteoritics & Planetary Science* 45:1302–1319.
- Ishii H. A. and Bradley J. P. 2006. Macroscopic subdivision of silica aerogel collectors for sample return missions. *Meteoritics & Planetary Science* 41:233–236.
- Ishii H. A., Graham G. A., Kearsley A. T., Grant P. G., Snead C. J., and Bradley J. P. 2005. Rapid extraction of dust impact tracks from silica aerogel by ultrasonic microblades. *Meteoritics & Planetary Science* 40:1741–1747.
- Ishii H. A., Bradley J. P., Dai Z. R., Chi M., Kearsley A. T., Burchell M. J., Browning N. D., and Molster F. 2008a. Comparison of comet 81P/Wild 2 dust with interplanetary dust from comets. *Science* 37:447–450.
- Ishii H. A., Brennan S., Bradley J. P., Pianetta P., Kearsley A. T., and Burchell M. J. 2008b. Sulfur mobilization in Stardust impact tracks (abstract #1561). 34th Lunar and Planetary Science Conference. CD-ROM.
- Jones S. M. 2007. A method for producing gradient density aerogel. *Journal of Sol-Gel Science and Technology* 44:255–258.
- Kawakita H., Watanabe J.-I., Ootsubo T., Nakamura R., Fuse T., Takato N., Sasaki S., and Sasaki T. 2004. Evidence of icy grains in comet C/2002 T7 (LINEAR) at 3.52 AU. *The Astrophysical Journal* 601:L191–L194.
- Kearsley A. T., Graham G. A., Burchell M. J., Taylor E. A., Drolshagen G., Chater R. J., and McPhail D. 2005. MULPEX: A compact multi-layered polymer foil collector for micrometeoroids and orbital debris. *Advances in Space Research* 35:1270–1281.
- Kearsley A. T., Burchell M. J., Hörz F., Cole M. J., and Schwandt C. S. 2006. Laboratory simulation of impacts upon aluminium foils of the Stardust spacecraft: Calibration of dust particle size from comet Wild 2. *Meteoritics & Planetary Science* 41:161–180.
- Kearsley A. T., Ball A. D., Graham G. A., Burchell M. J., Ishii H., Cole M. J., Wozniakiewicz P. J., Hörz F., and See T. H. 2007a. Aerogel track morphology: Measurement, three dimensional reconstruction and particle location using Confocal Laser Scanning Microscopy (abstract #1690). 38th Lunar and Planetary Science Conference. CD-ROM.
- Kearsley A. T., Graham G. A., Burchell M. J., Cole M. J., Dai Z. R., Teslich N., Bradley J. P., Chater R., Wozniakiewicz

- P. A., Spratt J., and Jones G. 2007b. Analytical scanning and transmission electron microscopy of laboratory impacts on Stardust aluminum foils: Interpreting impact crater morphology and the composition of impact residues. *Meteoritics & Planetary Science* 42:191–210.
- Kearsley A. T., Borg J., Graham G. A., Burchell M. J., Cole M. J., Leroux H., Bridges J. C., Hörz F., Wozniakiewicz P. J., Bland P. A., Bradley J. P., Dai Z. R., Teslich N., See T., Hoppe P., Heck P. R., Huth J., Stadermann F. J., Floss C., Marhas K., Stephan T., and Leitner J. 2008a. Dust from comet Wild 2: Interpreting particle size, shape, structure and composition from impact features on the Stardust aluminum foils. *Meteoritics & Planetary Science* 43:41–73.
- Kearsley A. T., Graham G. A., Burchell M. J., Cole M. J., Wozniakiewicz P., Teslich N., Branga E., Hörz F., Blum J., and Poppe T. 2008b. Micro-craters in aluminum foils on NASA's Stardust Spacecraft: Implications for dust particles emanating from Comet Wild 2. *International Journal of Impact Engineering* 35:1616–1624.
- Kearsley A. T., Burchell M. J., Price M. C., Graham G. A., Wozniakiewicz P. J., Cole M. J., and Teslich N. 2009. Interpretation of Wild 2 dust fine structure: Comparison of Stardust aluminium foil craters to the three-dimensional shape of experimental impacts by artificial aggregate particles and meteorite powders. *Meteoritics & Planetary Science* 44:1489–1511.
- Kearsley A. T., Burchell M. J., Price M. C., Green S. F., Franchi I. A., Bridges J. C., Starkey N., and Cole M. J. 2010. Distinctive impact craters are formed by organic-rich cometary dust grains (abstract #1435). 41st Lunar and Planetary Science Conference. CD-ROM.
- Kitazawa Y., Fujiwara A., Kadono T., Imagawa K., Okada Y., and Uematsu K. 1999. Hypervelocity impact experiments on aerogel dust collector. *Journal of Geophysical Research* 104:22035–22052.
- Leroux H., Rietmeijer F. J. M., Velbel M. A., Brearley A. J., Jacob D., Langenhorst F., Bridges J. C., Zega T. J., Stroud R. M., Cordier P., Harvey R. P., Lee M., Gounelle M., and Zolensky M. E. 2008. A TEM study of thermally modified comet 81P/Wild 2 dust particles by interactions with the aerogel matrix during the Stardust capture process. *Meteoritics & Planetary Science* 43:97–120.
- Lide D. R. (ed.). 2008 *CRC Handbook of Chemistry and Physics*. Boca Raton, FL: CRC Press, Taylor and Francis Group. 2688 p.
- Marcus M. A., Fakra S., Westphal A. J., Snead C. J., Keller L. P., Kearsley A., and Burchell M. J. 2008. Smelting of Fe-bearing glass during hypervelocity capture in aerogel. *Meteoritics & Planetary Science* 43:87–96.
- Niimi R., Kadono T., Arakawa M., Yasui M., Dohi K., Nakamura A. M., Iida Y., and Tsuchiyama A. 2011a. In situ observation of penetration process in silica aerogel: Deceleration mechanism of hard spherical projectiles. *Icarus* 211:986–992.
- Niimi R., Tsuchiyama A., Kadono T., Okudaira K., Hasegawa S., Tabata M., Watanabe T., Yagishita M., Machii N., and Nakamura A. M. 2011b. Dependence on projectile density of impact track morphology in silica aerogel (abstract #1934). 42nd Lunar and Planetary Science Conference. CD-ROM.
- Nixon A., Burchell M. J., Price M. C., Kearsley A. T., and Jones S. 2012. Aerogel tracks made by impacts of glycine: Implications for formation of bulbous tracks in aerogel and the Stardust mission. *Meteoritics & Planetary Science*. 47. This issue.
- Noguchi T., Nakamura T., Okudaira K., Yano H., Sugita S., and Burchell M. 2007. Thermal alteration of hydrated minerals during hypervelocity capture to silica aerogel at the flyby speed of Stardust. *Meteoritics & Planetary Science* 42:357–372.
- Okudaira K., Noguchi T., Nakamura T., Sugita S., Sekine Y., and Yano H. 2004. Evaluation of mineralogical alteration of micrometeoroid analog materials captured in aerogel. *Advances in Space Research* 34:2299–2304.
- Okudaira K., Yano H., Noguchi T., Nakamura T., Burchell M. J., and Cole M. J. 2005. Are they really intact? Evaluation of captured micrometeoroid analogs by aerogel at the flyby speed of Stardust (abstract #1832). 36th Lunar and Planetary Science Conference. CD-ROM.
- Price M. C., Kearsley A. T., Burchell M. J., Abel R., and Cole M. J. 2010a. Comet Wild 2 dust: How particle structure and composition are reflected in the shape of Stardust aerogel tracks (abstract #1313). 41st Lunar and Planetary Science Conference. CD-ROM.
- Price M. C., Kearsley A. T., Burchell M. J., Hörz F., Borg J., Bridges J. C., Cole M. J., Floss C., Graham G., Green S. F., Hoppe P., Leroux H., Marhas K. K., Park N., Stroud R., Stadermann F. J., Teslich N., and Wozniakiewicz P. J. 2010b. Comet 81P/Wild 2: The size distribution of finer (sub-10 μm) dust collected by the Stardust spacecraft. *Meteoritics & Planetary Science* 45:1409–1428. doi: 10.1111/j.1945-5100.2010.01104.x
- Sekanina Z., Brownlee D. E., Economou T. E., Tuzzolino A. J., and Green S. F. 2004. Modelling the nucleus and jets of comet 81P/Wild 2 based on the Stardust encounter data. *Science* 304:1769–1774.
- Speight J. G. 2005. *Handbook of coal analysis*. Hoboken, NJ: John Wiley & Sons Ltd. 240 p.
- Trigo-Rodríguez J. M., Dominguez G., Burchell M. J., Hörz F., and Llorca J. 2008. Bulbous tracks arising from hypervelocity capture in aerogel. *Meteoritics & Planetary Science* 43:75–86.
- Tsou P. 1990. Intact capture of hypervelocity projectiles. *International Journal of Impact Engineering* 10:615–627.
- Tsou P. 1995. Silica aerogel captures cosmic dust intact. *Journal of Non-Crystalline Solids* 186:415–427.
- Tsou P., Brownlee D. E., Laurance M. R., Hrubesh L., and Albee A. L. 1988. Intact capture of hypervelocity micrometeoroid analogs. Proceedings, 19th Lunar and Planetary Science Conference. pp. 1205–1206.
- Tsou P., Bradley J. P., Brownlee D. E., Fechtig H., Hrubesh F. L., Keaton P. W., Laurance M., Simon C. G., Stradling G. L., Teetsov A., and Albee A. L. 1990. Intact capture of cosmic dust analogs in aerogel (abstract). Proceedings, 21st Lunar and Planetary Science Conference. pp. 1264–1265.
- Tsou P., Brownlee D. E., Sandford S. A., Hörz F., and Zolensky M. E. 2003. Wild-2 and interstellar sample collection and earth return. *Journal of Geophysical Research* 108:8113, doi:10.1029/2003JE002109.
- Tsuchiyama A., Nakamura T., Okazaki T., Uesugi K., and Nakano T. 2009. Three-dimensional structures and elemental distributions of Stardust impact tracks using synchrotron microtomography and X-ray fluorescence analysis. *Meteoritics & Planetary Science* 44:1203–1224.
- Westphal A. J., Snead C., Borg J., Quirico E., Raynal P.-I., Zolensky M. E., Ferrini G., Colangeli L., and Palumbo P.

2002. Small hypervelocity particles captured in aerogel collectors: Location, extraction, handling and storage. *Meteoritics & Planetary Science* 37:855–865.
- Westphal A. J., Snead C., Butterworth A., Graham G. A., Bradley J. P., Bajt S., Grant P. G., Bench G., Brennan S., and Pianetta P. 2004. Aerogel keystones: Extraction of complete hypervelocity impact events from aerogel collectors. *Meteoritics & Planetary Science* 39:1375–1386.
- Wozniakiewicz P. J., Ishii H. A., Kearsley A. T., Burchell M. J., Bland P. A., Bradley J. P., Dai Z., Teslich N., Collins G. S., Cole M. J., and Russell S. S. 2011. Investigation of iron sulfide impact crater residues: A combined analysis by scanning and transmission electron microscopy. *Meteoritics & Planetary Science* 46:1007–1024.
- Wozniakiewicz P. J., Kearsley A. T., Ishii H. A., Burchell M. J., Bradley J. P., Price M. C., Teslich N., Lee M. R., and Cole M. J. 2012. Stardust impact analogues: Resolving pre- and post-impact mineralogy in Stardust Al foils. *Meteoritics & Planetary Science* 47. This issue.
- Yano H., Arakawa M., Michikami T., and Fujiwara A. 1999. Sub-millimeter sized ice grain impacts on aerogels; implications to a cometary dust sample return mission (abstract #1961). 30th Lunar and Planetary Science Conference. CD-ROM.
- Zolensky M. E., Barrett R. A., Hrubesh L., Hörz F., and Lindstrom D. 1990. Cosmic dust capture simulation experiments using silica aerogels. Proceedings, 21st Lunar and Planetary Science Conference. pp. 1381–1382.
- Zolensky M. E., Zega T. J., Yano H., Wirick S., Westphal A. J., Weisberg M. K., Weber I., Warren J. L., Velbel M. A., Tsuchiyama A., Tsou P., Toppani A., Tomioka N., Tomeoka K., Teslich N., Taheri M., Susini J., Stroud R., Stephan T., Stadermann F. J., Snead C. J., Simon S. B., Simionovici A., See T. H., Robert F., Rietmeijer F. J. M., Rao W., Perronnet M. C., Papanastassiou D. A., Okudaira K., Ohsumi K., Ohnishi I., Nakamura-Messenger K., Nakamura T., Mostefaoui S., Mikouchi T., Meibom A., Matrajt G., Marcus M. A., Leroux H., Lemelle L., Le L., Lanzirotti A., Langenhorst F., Krot A. N., Keller L. P., Kearsley A. T., Joswiak D., Jacob D., Ishii H., Harvey R., Hagiya K., Grossman L., Grossman J. N., Graham G. A., Gounelle M., Gillet P., Genge M. J., Flynn G., Ferroir T., Fallon S., Ebel D. S., Dai Z. R., Cordier P., Clark B., Chi M., Butterworth A. L., Brownlee D. E., Bridges J. C., Brennan S., Brearley A., Bradley J. P., Bleuet P., Bland P. A., and Bastien R. 2006. Mineralogy and petrology of comet Wild 2 nucleus samples. *Science* 314:1735–1739.
- Zolensky M., Nakamura-Messenger K., Rietmeijer F., Leroux H., Mikouchi T., Ohsumi K., Simon S., Grossman L., Stephan T., Weisberg M., Velbel M., Zega T., Stroud R., Tomeoka K., Ohnishi I., Tomioka N., Nakamura T., Matrajt G., Joswiak D., Brownlee D., Langenhorst F., Krot A., Kearsley A., Ishii H., Graham G., Dai Z. R., Chi M., Bradley J., Hagiya K., Gounelle M., Keller L., and Bridges J. 2008. Comparing Wild 2 particles to chondrites and IDPs. *Meteoritics & Planetary Science* 43:261–272.